

LATVIAN
JOURNAL
of
PHYSICS
and TECHNICAL
SCIENCES

ISSN 0868 - 8257

2

(Vol. 54)

2017

Ind. pasūt. € 1,50
Org. € 15,00

Indekss 2091
Indekss 2092

SATURS

ENERĢĒTIKAS FIZIKĀLĀS UN TEHNISKĀS PROBLĒMAS

Serebrjakovs A., Kamoliņš E., Levins N. <i>Elektriskais ģenerators transportlīdzekļu svārstību slāpēšanas sistēmā</i>	3
Dirba J., Lavrinoviča L., Dobrijans R. <i>Sinhrono ventiļdzinēju darba īpatnības servodzinēju režīmos</i>	14
Kauškale L., Geipele I., Zeltiņš N., Lecis I. <i>Būvniecības nozares vides un enerģētikas aspekti, un zaļā būvniecība</i>	24

FIZIKA

Kanders U., Kanders K. <i>Vakuuma pārklājumu substrātu nanoindentēšanas datu analīze-II: Uzkaldināšanas-atkaldināšanas oscilācijas pievirsmas slānī</i>	34
---	----

LIETIŠĶĀ FIZIKA

Bulaha N., Rudzītis J., Lungevičs J., Liniņš O., J.Krizbergs J. <i>Virsmas raupjuma anizotropijas izpēte</i>	46
Rudzītis J., Bulaha N., Lungevičs J., Liniņš O., Bērziņš K. <i>Anizotropā 3D virsmas raupjuma soļa parametru teorētiskā analīze</i>	55
Leitāns A., Lungevičs J., Rudzītis J., Fiļipovs A. <i>PVD Ti/C-N nanopārklājumu triboloģiskās īpašības</i>	64

ĪSAIS ZIŅOJUMS

Kalnačs A. <i>Projekta Baltic Flows rezultāti</i>	72
---	----

Price to individual subscribers € 1.50/issue
Price to collective subscribers € 15.00/issue

Index 2091
Index 2092

CONTENTS

PHYSICAL AND TECHNICAL ENERGY PROBLEMS

Serebryakov A., Kamolins E., Levin N. <i>Electric generator in the system for damping oscillations of vehicles</i>	3
Dirba J., Lavrinovicha L., Dobriyan R. <i>Features of synchronous electronically commutated motors in servomotor operation modes</i>	14
Kauskale L., Geipele I., Zeltins N., Lecis I. <i>Environmental and energy aspects of construction industry and green buildings</i>	24

PHYSICS

Kanders U., Kanders K. <i>Nanoindentation response analysis of thin film substrates-II: Strain hardening-softening oscillations in subsurface layer</i>	34
---	----

APPLIED PHYSICS

Bulaha N., Rudzitis J., Lungevics J., Linins O., Krizbergs J. <i>Research of surface roughness anisotropy</i>	46
Rudzitis J., Bulaha N., Lungevics J., Linins O., Berzins K. <i>Theoretical analysis of spacing parameters of anisotropic 3D surface roughness</i>	55
Leitans A., Lungevics J., Rudzitis J., A.Filipovs <i>Tribological properties of PVD Ti/C-N nanocoatnigs</i>	64

SHORT REPORT

Kalnach A. <i>Results of Baltic Flows Project</i>	72
---	----

Индивид. заказ. € 1,50
Орг. заказ. € 15,00

Индекс 2091
Индекс 2092

СОДЕРЖАНИЕ

ФИЗИКО-ТЕХНИЧЕСКИЕ ПРОБЛЕМЫ ЭНЕРГЕТИКИ

Серебряков А., Камолиныш Е., Левин Н. <i>Электрический генератор в системе демпфирования колебаний транспортных средств</i>	3
Дирба Я., Лавриновича Л., Добриян Р. <i>Особенности синхронных электронно-коммутируемых двигателей в режимах работы серводвигателей</i>	14
Каушкале Л., Гейпеле И., Зелтиньш Н., Лецис И. <i>Экологические и энергетические аспекты строительной отрасли и зеленых зданий</i>	24

ФИЗИКА

Кандерс У., Кандерс К. <i>Анализ характеристик наноиндендирования тонкопленочной подложки- II: Деформационно-упрочняющие и размягчающие колебания в приповерхностном слое</i>	34
---	----

ПРИКЛАДНАЯ ФИЗИКА

Булаха Н., Рудзитис Я., Лунгевич Я., Линин О., Кризберг Ю. <i>Исследование анизотропии шероховатости поверхности</i>	46
Рудзитис Я., Булаха Н., Лунгевич Я., Линин О., Берзиньш К. <i>Теоретический анализ интервальных параметров анизотропной трехмерной шероховатости поверхности</i>	55
Лейтанс А., Лунгевич Я., Рудзитис Я., Филипов А. <i>Трибологические свойства наноразмерных пленок PVD Ti/C-N</i>	64

КРАТКОЕ СООБЩЕНИЕ

Калнач А. <i>Результаты проекта Baltic Flows</i>	72
--	----

LATVIAN
JOURNAL
of
PHYSICS
and TECHNICAL
SCIENCES

LATVIJAS
FIZIKAS
un TEHNISKO
ZINĀTŅU
ŽURNĀLS

ЛАТВИЙСКИЙ
ФИЗИКО-
ТЕХНИЧЕСКИЙ
ЖУРНАЛ

Published six times a year since February 1964
Iznāk sešas reizes gadā kopš 1964. gada februāra
Выходит шесть раз в год с февраля 1964 года

2 (Vol. 54) • 2017

RĪGA

REDAKCIJAS KOLĒGIJA

I. Oļeņikova (galv. redaktore), A. Ozols, A. Mutule, J. Kalnačs, A. Siliņš,
G. Klāvs, A. Šarakovskis, M. Rutkis, A. Kuzmins, Ē. Birks, S. Ezerniece (atbild.
sekretāre)

KONSULTATĪVĀ PADOME

J. Vilemas (Lietuva), K. Švarcs (Vācija), J. Kapala (Polija), J. Melngailis (ASV),
T. Jēskelainens (Somija), J. Savickis (Latvija), N. Zeltiņš (Latvija), Ā. Žīgurs (Latvija)

EDITORIAL BOARD

I. Oleinikova (Chief Editor), A. Ozols, A. Mutule, J. Kalnacs, A. Silins, G. Klavs, A.
Sarakovskis, M. Rutkis, A. Kuzmins, E. Birks, S. Ezerniece (Managing Editor)

ADVISORY BOARD

Yu. Vilemas (Lithuania), K. Schwartz (Germany), J. Kapala (Poland), J. Melngailis
(USA), T. Jeskelainens (Sweden), J. Savickis (Latvia), N. Zeltinsh (Latvia), A. Zigurs
(Latvia)

Korektore: O. Ivanova
Maketētājs I. Begičevs

INDEKSĒTS (PUBLICĒTS) | INDEXED (PUBLISHED) IN

www.scopus.com

www.degruyter.com

EBSCO (Academic Search Complete, www.epnet.com), INSPEC (www.iee.org.com).

VINITI (www.viniti.ru), Begell House Inc/ (EDC, www.edata-center.com).

Izdevējs: Fizikālās enerģētikas institūts
Reģistrācijas apliecība Nr. 0221
Redakcija: Krīvu iela 11, Rīga, LV-1006
Tel. 67551732, 67558694
e-pasts: ezerniec@edi.lv
Interneta adrese: www.fei-web.lv
Iespiests SIA "AstroPrint"

ELECTRIC GENERATOR IN THE SYSTEM FOR DAMPING
OSCILLATIONS OF VEHICLES

A. Serebryakov, E. Kamolins

Riga Technical University

12/1 Azenes Str., Riga, LV-1048, LATVIA

e-mail: edmunds.kamolins@rtu.lv

N. Levin

Institute of Physical Energetics

11 Krivu Str., Riga, LV-1006, LATVIA

The control systems for the objects of industry, power generation, transport, etc. are extremely complicated; functional efficiency of these systems determines to a great extent the safe and non-polluting operation as well as convenience of service and repair of such objects. The authors consider the possibility to improve the efficiency of systems for damping oscillations in transport using a combination of electrical (generators of rotational and linear types) and hydraulic means. Better efficiency of functioning is achieved through automatic control over the operational conditions of such a system in order to make it adaptive to variations in the road profile and ambient temperature; besides, it is possible to produce additional electric energy.

Keywords: *damping system, hydraulic damper, permanent magnet generators.*

1. INTRODUCTION

The contemporary technical objects are complex aggregates of elements that should operate reliably fulfilling all the functions to ensure their normal operation. This relates to all kinds of technical means, including transport [1]–[3].

For example, in a usual car that runs on a low-quality motor road the oscillations of its frame and body not only make the driving more complicated, but also jeopardize the safety of traffic; they introduce discomfort to the passengers, and, besides, can cause damage to the car itself as well as to the transported freight.

Therefore, these oscillations should be damped, which is done with the help of special elements of the car suspension – suspension dampers (shock absorbers) [4]. Hydraulic (oil) dampers are among the most widespread elements used for this purpose.

The efficiency of a hydro-damping system can be raised by introducing special electric generators into it. This would allow carrying away heat losses due to oscillations beyond the limits of hydraulics, thus saving it from overheating and making it possible to receive an extra source of electric energy.

In this case, utilisation of the oscillation energy and its conversion into the electric one happen simultaneously.

Apart from that, a possibility arises for fast adaptation of a damping system to the variations in the road conditions, running speed, and ambient temperature. Such a possibility is considered below.

2. ELECTRIC GENERATOR IN THE SYSTEM FOR DAMPING OSCILLATIONS IN A CAR

In order to justify the above-mentioned statements, in Fig. 1 a block diagram of structural design is shown for a combined electro-hydraulic system for damping oscillations in a car. The figure displays: spring (1), with which and with car body (2) hydro-pump (3) with plunger (4) are rigidly connected. Rack of the chassis (5) is linked to hydro-pump plunger (4) and spring (1). With both cavities of hydro-pump (3) through hydro-distributor (7), hydro-motor (8) is connected, which brings electro-generator (9) into rotation.

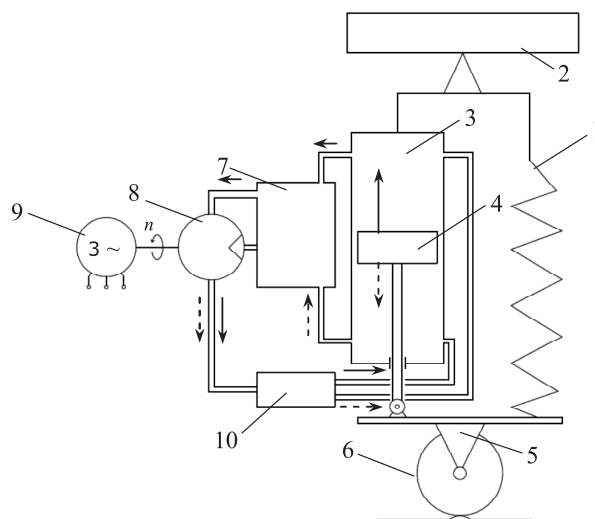


Fig. 1. Block diagram of structural design of the system for damping the car oscillations with rotational (type) electric generator: 1 – spring; 2 – car body; 3 – hydro-pump; 4 – plunger; 5 – rack of the chassis; 6 – wheel; 7 – hydro-distributor; 8 – hydro-motor; 9 – electric generator; 10 – compensative capacities.

The scheme operates as follows: when wheel (6) is running over road asperity, spring (1) is compressed, and plunger (4) in hydro-pump (3) is going up. The oil (hydraulic liquid) is squeezed out of the upper cavity of hydro-pump (3) through hydro-distributor (7) into hydro-motor (8). At reverse movement of the plunger (i.e., down), after the wheel has run down from the obstacle, the oil from the lower ca-

vity of hydro-pump (3) enters the hydro-motor – the same cavity that in the previous case. As a result, the hydro-motor is rotating in one and the same direction – independently of the plunger movement. The oil that under high pressure finds its way into the hydro-motor ensures the required rotational speed for it (and, respectively, for the electro-generator), thus transforming the kinetic energy of oil motion into the rotational movement of the generator rotor, overcoming its electro-magnetic resistance moment. The working process is controlled by the hydro-distributor (7). Compensative capacities (10) provide, respectively, discharging of excessive oil and replenishing the deficient oil in the cavities of hydro-pump. Hence, the latter is here functioning as a hydro-absorber.

To demonstrate the efficiency of the damping system under consideration, we will describe its operation mathematically, using a differential equation. For simplicity, the following assumptions have been made:

- all the forces and movements in the system are directed vertically (along the y -axis);
- the forces and movements directed along other coordinate axes (x, z) do not affect the process that is going in the y -direction;
- the temperature, magnetic and mechanical effects exerted on the system in the direction of variations in its parameters are ignored;
- the curve of spring rate is linearized, its value is constant and takes into account the processes going in the pneumatic system of wheels;
- the viscosity of oil and the geometrical sizes of individual system elements – along with the friction coefficient – are assumed to be constant;
- the mutual influence of wheels and of related masses is absent.

Taking into account the above-mentioned assumptions, the expression for acceleration of the car body movements as related to one wheel can be written as follows:

$$\frac{d^2(y_t - y_0)}{dt^2} = \frac{G - F_c - F_a - F_g - F_l}{m}. \quad (1)$$

Here G is the weight of the car part that falls on one wheel, N, and m is its mass, kg;

$F_c = c_y(y_t - y_0)$ is the opposing force of spring at shifting the point y_t of its fastening to the body relative to original point y_0 of equilibrium state, N; C_y is the spring rate, N/m;

$F_a = \frac{2iC\Phi(C\Phi V_r - U)}{D\sqrt{R_a^2 + X_a^2}}$ is the maximum opposing circumferential force of generator as related to the piston rod, where i is the reduction coefficient determined by hydraulic transmission of the force; C is a design constant of the generator; Φ is the magnetic flux, Wb; V_r is the circumferential speed of generator rotor, m/s; D is

the rotor diameter, m; $R_a + jX_a = Z_a$ is the complex adjustable resistance connected between the generator and the accumulator cell, Ω ; U is the voltage of accumulator cell, V;

$F_g = K_g \frac{dy}{dt}$ is the friction force due to hydraulic line, N, with K_g being the friction coefficient, Ns/m;

F_l is the occasional force stemming from collision of wheel with the roadway covering, N; this chaotic and short-term force upsets the balance of car body-spring-absorber system with deviation y .

Taking into account the character of action of force F_l and the absence of re-covering force, the oscillations arising in the system are free and damped.

Substitution of the above components into Eq. (1), taking into account that in the equilibrium state $G = C_y y_0$, gives a finite differential equation for the car body movements in the form:

$$\frac{d^2 y}{dt^2} + \left[\frac{2iC\Phi(C\Phi V_r - U)}{Dm\sqrt{R_a^2 + X_a^2}} + \frac{K_g}{m} \right] \frac{dy}{dt} + \frac{C_y}{m} y = \pm \frac{F_l}{m}. \quad (2)$$

The characteristic equation describing free oscillations after occasional road shock takes the form:

$$y^2 + \left[\frac{2iC\Phi(C\Phi V_r - U)}{Dm\sqrt{R_a^2 + X_a^2}} + \frac{K_g}{m} \right] y + \frac{C_y}{m} = 0. \quad (3)$$

The roots of Eq. (3) will thus be:

$$P_{1,2} = \pm j \sqrt{\frac{C_y}{m} - \left[\frac{iC\Phi(C\Phi V_r - U)}{Dm\sqrt{R_a^2 + X_a^2}} + \frac{K_g}{2m} \right]^2} - \frac{iC\Phi(C\Phi V_r - U)}{Dm\sqrt{R_a^2 + X_a^2}} + \frac{K_g}{2m}. \quad (4)$$

Solution of equation (3) will have the form:

$$y = (Y_0 - y_0) e^{-kt} \cos \omega_0 t, \quad (5)$$

where $(Y_0 - y_0) = y_m$ is the maximum deviation of the car body from the equilibrium state as a result of occasional road shock at time t_0 (the beginning of the process), with Y_0, y_0 being the car body ordinates relative to the lower fastening point of spring before and after car running over the obstacle (Fig. 2).

In Eq. (5):

$$k = \left[\frac{iC\Phi(C\Phi V_r - U)}{Dm\sqrt{R_a^2 + X_a^2}} + \frac{K_g}{2m} \right] - \quad (6)$$

is the coefficient of oscillation damping, and

$$\omega_0 = \sqrt{\frac{C_y}{m} - \left[\frac{iC\Phi(C\Phi V_r - U)}{Dm\sqrt{R_a^2 + X_a^2}} + \frac{K_g}{2m} \right]^2} \quad (7)$$

is the natural angular frequency of undamped continuous oscillations.

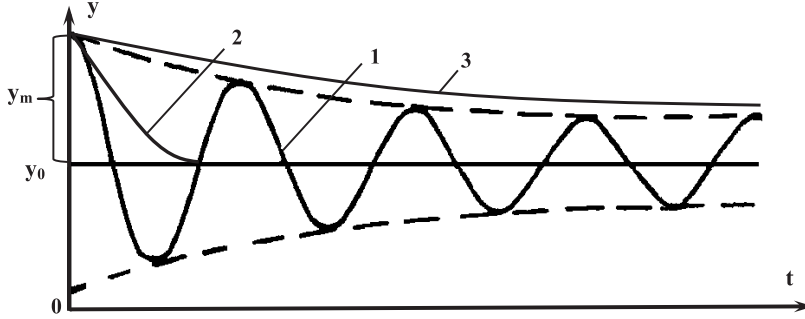


Fig. 2. Oscillation curves for different parameters of the damping system.

Inferences that could be drawn based on the analysis of expressions (5–7) are as follows:

- The parameters of the electro-hydraulic damping system exert influence on the formation of body movement process. In Fig. 2, the curves of possible processes of the type are plotted: curve 1 – for the damped vibrations at $k > 0$, $\omega_0 > 0$; curve 2 – for the limiting case of periodic movement at $\omega_0 = 0$, $k > 0$; curve 3 – for the asymptotic movement at $k = 0$, $\omega_0 = 0$.
- Each of these transient processes can be implemented varying the impedance Z_a or magnetic flux of generator Φ . This could be done automatically, with the help of generator while the car is running, by setting the most favourable at the given motion speed, road covering quality, and ambient temperature.
- By adjusting the system for damping vibrations, it is possible to avoid the resonance phenomena, thus excluding consequences of emergency situations; besides, the operation at low-frequency vibrations (dangerous to human life) is ruled out, which increases the efficiency of the damping system.
- The controlled adaptation of the system to ambient temperature variations also increases the system efficiency. This is achieved varying the power of generator, and, correspondingly, the elastance rate of the electrical part of combined absorber under winter and summer conditions. Thus, at freezing weather the oil thickens, its viscosity increases; this makes the hydro-absorber more rigid; correspondingly, the car motion smoothness becomes worse. Such being the case, decreasing the elastance rate of the electrical part of combined absorber at the cost of decreased generator

power would weaken the impact of low temperature. Vice versa, under high summer temperatures the oil becomes less viscous, while the hydro-damper – softer, the road grip of a wheel is worsening, and, therefore, the road safety also becomes worse. In this case, increase in the rigidity of damper due to greater power of generator will moderate the effect of high temperature.

- One and the same obstacle on the road produces different action on the damping system. At a high running speed this action might be stronger, which at constant rigidity of damping system would lead to a greater vibration amplitude, weaker road grip of the wheels, worse safety and comfort of travel, etc. The same occurs at the speed being slower but the obstacle higher. However, raising the power of generator moderates the action of these factors, and will, therefore, serve to improve the damping system performance.

A deeper analysis of Eqs. (5–7) might result in discovery of other important factors; for example, when the oil is too viscous while the friction coefficient is increasing the system becomes uncontrollable and passes to aperiodic operational condition. Such being the case, no additional electric energy is produced. Another example is dealing with a spring of high rigidity, when the damping system passes to the operation with constant oscillations of elevated frequency and amplitude, which might cause excessive discomfort for the passengers and damage to the transported freight – especially if the roadway is with gravel or cobble-stone covering.

All the mentioned nuances should be taken into account when designing the damping systems and their operation.

At the same time, if such a system provides a combined electro-hydraulic control of damping oscillations of cars or other identical objects (buses, railway vans, etc.), its use simplifies to a great extent the problem of achieving better performance for a damping system, making it also possible to derive extra electric energy due to operation of a generator in this combined system.

One of the benefits of a combined system for damping vibrations with a generator of rotational type is the possibility to dispose separately its elements: the hydro-cylinder on chassis, while the hydro-motor, the hydraulic control valve and the electric generator – inside the car body. This would significantly simplify the implementation of the damping system and its operation.

3. DESIGN OF THE ELECTRIC GENERATOR FOR EFFICIENT DAMPING OSCILLATIONS AND UTILISATION OF THEIR ENERGY

In order to make a judicious selection among the designs of a generator as part of the combined system for damping the car body oscillations and utilisation of their energy, it is necessary to define the criteria for such a selection.

The electric machines employed in modern vehicles are usually subject to severe conditions. These could be: jolting, vibrations, impact loads, varying ambient temperatures and humidity, operation under the action of aggressive media as well as of electric and magnetic fields – that is, under unfavourable conditions.

Taking all this into account, it is necessary that the design of generator is the simplest and most reliable, providing a high specific torque (force), improved thermal stability – and, therefore, wide possibilities for the use of low-temperature permanent magnets with high enough specific energy, and to meet many other requirements that are not imposed upon electric machines working under standard conditions.

The electric generator to be used in a car damping system should be a power element that would be capable of developing a damping force comparable with the weight of this car as related to one wheel, i.e., several hundreds of newtons. Therefore, it is of little sense to use a gearless direct-driven generator – mainly due to big forces and low rates of magnetic-flux linkage of windings with magnetic field.

Since the mass of an electric machine is determined by its electro-magnetic force (torque), the generator is to be used in a high-speed condition. This means that such a generator should have a gear for decreasing the output speed and increasing the force applied to the rod, which would counteract the pressure applied to the spring. Under these conditions, it is expedient for excitation of the generator to use permanent magnets, which should be reliably protected from overheating. Such a protection can be provided by placing the magnets on the rotor, while the armature winding – on the stator.

It is tempting in many cases that execution of generator is direct-driven and linear. But then on the stator both the magnets and the winding must be placed, which would substantially complicate the use of low-temperature permanent magnets; besides, in this case the machine must be of inductor type, i.e., of much worse efficiency due to the edge effect typical of electric machines with open-chain magnetic circuit.

Thus, for example, if length l of the mobile part of the generator is comparable with its width b ($l/b \leq 3-4$), the efficiency decreases from 0.8 to 0.6 as in a conventional electric machine [5]–[7].

Under these conditions for a direct-driven generator special design solutions are required, which would provide better cooling of the generator and raise its linear load.

Therefore, the following rational design stands out for a rotational type of generator: a multipole rotor with permanent magnets from magnetically hard material (e.g., NdFeB); a stator that is capsulated in order to separate it thermally from the rotor which might have between the magnets and the shaft an impeller, i.e., a turbine for intensive heat removal from the generator.

The calculated version of the considered design of eight-pole generator has the following main technical indicators:

- rotor diameter and length – 0.75 m ;
- rotational speed $n = 3000\text{ min}^{-1}$;
- nominal power $P = 0.5\text{ kW}$;
- electromechanical torque $M_{em} = 1.6\text{ N} \cdot \text{m}$;
- radial force of the generator $F = 40\text{ N}$;
- mass of the generator $G = 3.8\text{ kg}$;
- specific power $P_{sp} = 140\text{ W} / \text{kg}$.

Linear generators [8]–[10] can also be used in a car damping system. The arrangement of the damping system (Fig. 3) in this case is much simpler than in the system with a rotating generator (Fig. 1). However, due to low specific parameters of linear generators [11]–[13] compared to rotating generators (3÷4 times or more) the linear generator application in the direct damping system is not always rational.

It should be noted that – despite lower indices of linear electric machines (LEMs) as compared to machines of rotational type – these former generators are conveniently arranged in the suspension of a vehicle and, in principle, are able to operate at reciprocating movements of the mobile part. This means that LEMs can be used for creation of active adaptive systems to damp the oscillations of a car.

For instance, SKF company has worked out the suspension with a spring as the elastic element, and absorber in the form of a linear generator as the damping one [14].

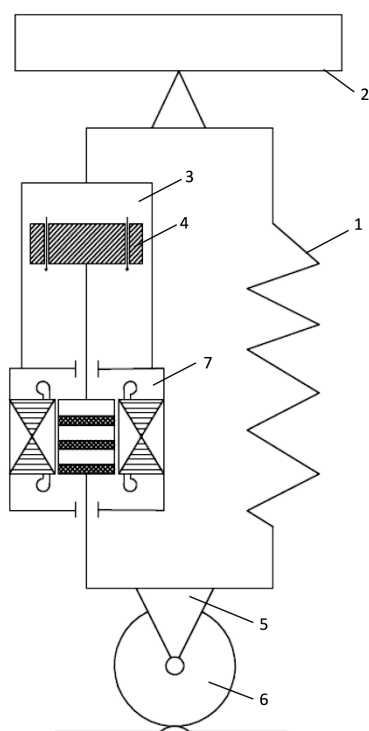


Fig. 3. Block diagram of structural design of the system for damping the car oscillations with linear (type) electric generator: 1 – spring; 2 – car body; 3 – hydro-absorber; 4 – plunger; 5 – rack of the chassis; 6 – wheel; 7 linear generator.

To control the operation of absorber, a controller is used, which contains sensors providing data on the road condition, motion speed, ambient temperature, etc.; the corresponding information is computer-processed, while the received signal is used for control over the absorber. In addition, the energy of vibrations is converted into the electric energy.

In turn, BOSE Company used an electric machine as the electro-magnetic suspension; the essence of this design is that instead of a spring and an absorber there is a controller-operated LEM [15].

The active suspension systems made it possible to significantly improve the efficiency of such systems to be used in cars. However, serious flaws – complexity, considerable energy consumption, high cost – discourage the use of adaptive suspensions in all types of transport, and so far they find application only in expensive top-class cars.

It is, therefore, reasonable to consider in this paper simpler and cheaper damping systems with combined absorbers whose application is possible in a wide range of vehicles.

The most important requirement for the electric machines to be used in active suspension systems is the possibility to control their operational modes with maximum speed of response; taking into account that such machines operate in unsteady transient conditions (in the motoring mode – starting-up, braking, reversing, variations in the load moment and rotational speed, while in the generator mode – variations in the load torque, power, rotational frequency, and in the motion speed of mobile part) the required speed of response is ≤ 1 ms. This means that these electric machines are to be controllable.

4. CONCLUSIONS

The method considered in the paper is based on the combination of electrical and hydraulic parts in the damping system. According to this method, the damping is performed both at the cost of energy loss in the hydraulic part and removal of this energy beyond the hydraulics, using for this purpose an electric generator. Therefore, the hydraulic part presents one of the channels for transformation of oscillation energy into heat, and is the reduction gear of a type to be used for ensuring the serviceability of the electrical channel for damping oscillation.

The main benefits to be derived from the use of such a combined system are the following:

- possibility to control the operational condition of the system through the use of electric generator by varying the power of which the system automatically adapts to unsteady conditions of transport motion: its speed, the road quality, ambient temperature, etc. Thus, better efficiency of the system is achieved during transportation – comfort and safety of passengers, preservation of freight; besides, additional electric energy is produced;
- partial heat removal beyond the hydraulics with the help of the electrical part of the system and, therefore, its higher reliability at the cost of lesser oil overheating in its hydraulic part;
- inadmissibility of the system operation at low-frequency vibrations that are dangerous for the life of people as well as at resonance (phenomena) that can cause an emergency situation;
- accessibility and simplicity of the control over the system operational conditions by varying the braking torque of generator;
- reduced costs of operation owing to smaller wear of the system components;
- saving the car resources at the cost of better operational conditions;

- increase in the volume of freight-passenger transportation owing to the improved availability (factor) of the car for operation.

REFERENCES

1. Vinogradov, R. I., & Ponamerov, A. N. (1991). *Development of World Aircrafts* (in Russian). Moscow: Mechanical Engineering.
2. Twidell, J., & Weir, T. (1986). *Renewable Energy Resources*. London: Routledge.
3. Tamoyan, G.S., Afonin, M.V., Sokolova, E.M., & Myo Tet Thu. (2007). Perspectives of the synchronous generators with the permanent magnets and reciprocation of an inductor (in Russian). *Elektrichestvo*, 16, 54–56.
4. Raympel, Y. (1986). *Car Chassis. Shock Absorbers, Tires and Wheels* (in Russian). Moscow: Mechanical Engineering.
5. Sturman, G. I. (1975). Induction machines with an open magnetic circuit (in Russian). *Elektrichestvo*, 10.
6. Levin, N. N., & Sturman, G. I. (1966). *Multi-Pole Synchronous Machine with an Open Magnetic Circuit* (in Russian). Moscow: VNIIEB BEM. (No. 1).
7. Levin, N. N., & Sturman, G. I. (1964). *Multiphase Inductor Machines in an Arc and Flat Design* (in Russian). Riga: Brushless Electrical Machines. (No. 3).
8. Hiterer, M. Y., & Ovchinnikov, I. E. (2008). *Synchronous Electric Machines with Reciprocating Motion* (in Russian). Sankt-Peterburg: Korona print.
9. Visocky, V. E. (2010). Linear permanent magnet generator for power supply systems of autonomous objects (in Russian). *Mechanical Engineering*, 1, 80–82.
10. Budikova, N. L., Sattarov, R. R., & Polihach, E. A. (2009). To the question of classification of linear electric generators (in Russian). *Gazette of Ufa State Aviation Technical University*, 12(2), 145–149.
11. Visocky, V. E., Tarashev, S. A., Sinicin, A. P., Zlobina, E. K., & Minenko, S. I. (2012). Development and design of linear permanent magnet generators for autonomous electric power systems (in Russian). *Southern Federal University Engineering Science*, 128(3).
12. Kecaris, A. A., & Duhanin, V. I. (2010). Linear generator issues with a workflow reciprocating (in Russian). In the 77th International Scientific and Technical Conference (pp. 36–42). Moscow: Moscow State Technical University.
13. Visocky, V. E., Shamesmuhometov, S. L., & Staruhin, A. A. (2010). *Forming Computational Model for Determining the Basic Characteristics and Parameters of the Linear Generator with Permanent Magnets* (in Russian). Samara: Samara State Technical University.
14. Terehov, I. (2011). *Dutch scientists have developed an electromagnetic suspension for cars* (in Russian). Retrieved 6 March 2017, from <https://3dnews.ru/609190>.
15. Shuldiner, H. (2007). *Bose says suspension drawing interest from OEMs*. Retrieved 6 February 2017, from <http://wardsauto.com>.

ELEKTRISKAIS ĢENERATORS TRANSPORTLĪDZEKĻU SVĀRSTĪBU SLĀPĒŠANAS SISTĒMĀ

A. Serebrjakovs, E. Kamoliņš, N. Levins

K o p s a v i l k u m s

Vadības sistēmas rūpniecībā, enerģētikā, transportā u.c. ir ļoti sarežģītas un to funkcionēšanas efektivitāte nosaka ekspluatācijas drošumu, apkārtējās vides tīrību, ekspluatācijas un remonta ērtumu. Autori apsver iespēju uzlabot transportlīdzekļu svārstību sistēmas funkcionēšanas efektivitāti, pielietojot kombinētus elektriskos (rotējošus un lineārus ģeneratorus) un hidrauliskos līdzekļus. Funkcionēšanas efektivitātes paaugstināšana tiek nodrošināta ar automātisku svārstību sistēmas režīma regulēšanu atbilstoši ceļa profilam un apkārtējās vides temperatūrai, kā arī nodrošinot papildus elektroenerģijas izstrādi.

07.03.2017.

DOI: 10.1515/lpts-2017-0009

FEATURES OF SYNCHRONOUS ELECTRONICALLY COMMUTATED MOTORS IN SERVOMOTOR OPERATION MODES

J. Dirba, L. Lavrinovicha, R. Dobriyan
Riga Technical University,
12/1 Azenes Str., Riga, LV-1048, LATVIA
e-mail: janis.dirba@rtu.lv

The authors consider the features and operation specifics of the synchronous permanent magnet motors and the synchronous reluctance motors with electronic commutation in servomotor operation modes. Calculation results show that mechanical and control characteristics of studied motors are close to a linear shape. The studied motor control is proposed to implement similar to phase control of induction servomotor; it means that angle θ (angle between vectors of the supply voltage and non-load electromotive force) or angle ε (angle between rotor direct axis and armature magnetomotive force axis) is changed. The analysis results show that synchronous electronically commutated motors could be used as servomotors.

Keywords: *servomotor; synchronous reluctance motor; synchronous permanent-magnet motor.*

1. INTRODUCTION

Servomotors are widely used in many devices and systems, for example, robotic systems, surveillance systems, automatic control systems, gyroscopic devices and others. Considering specific conditions of servomotor operation, there are different requirements for their characteristics compared to classical electric motors. The main requirements are the following: possibility to control rotation speed over wide range, linearity of mechanical and control characteristics, low inertia, adequate starting characteristics, stable rotor position according to the control signal and some others. As it is known, the most suitable motor type to be used in the role of servomotor is brushed DC motor. Such motors have the most suitable characteristics; however, their design is complex, and they have high maintenance costs, high electrical and mechanical losses, as well as insufficient safety. Brush-collector unit in its construction generally causes the described disadvantages of brushed DC motors [1]–[3].

The brushless synchronous electrical motors (synchronous permanent magnet motors and synchronous reluctance motors) are considered a good alternative to brushed motors due to their high safety level and other advantages [4]–[10].

Synchronous permanent magnet motors have such disadvantages as a high

cost of permanent magnets and high electromagnetic torque ripple. High electromagnetic torque ripple of such motors results from the cogging torque due to the interaction between the permanent magnets of the rotor and the stator slots. In comparison with synchronous permanent magnet motors, synchronous reluctance motors have low value of the electromagnetic power (torque) per unit volume. Moreover, synchronous reluctance motors also have high electromagnetic torque ripple that, in that case, is the result of the rotor magnetic asymmetry.

Synchronous reluctance motors have neither winding of excitation nor permanent magnets, which is why they are safer and cheaper in comparison with other types of electric motor. The operation principle of synchronous reluctance motor is based on a deep variation in the magnetic flux due to different reluctance on its way.

The aim of the paper is to study features and application possibilities of synchronous electronically commutated motors in servomotor operation modes.

2. CONTROL FEATURES OF DIRECT CURRENT AND ALTERNATING CURRENT SERVOMOTORS

Direct current (DC) and alternating current (AC) motors are widely used in servomotor operation modes. From the perspective of control method, DC servomotors can be divided into servomotors with anchor control and that with pole control. Servomotors with anchor control have constant excitation current value, while control possibility is based on change of anchor winding voltage U_c value and direction. In this case, shapes of characteristics $T = f(U_c)$ and $\omega = f(U_c)$ are linear. Since excitation current is constant, in some cases excitation winding can be replaced with permanent magnets.

Anchor winding of servomotors with pole control is supplied with constant voltage value, so the excitation winding – with control voltage U_c . This requires less control power; however, characteristics $\omega = f(U_c)$ are no longer linear. That is why anchor control is often used. The use of hollow non-magnetic or slotless anchor with pressed winding in DC servomotor increases possibility of stable high-speed control.

Of all AC servomotors, single-phase induction motors are used more often. Control of single-phase induction servomotors is implemented by three methods. The first method is amplitude control. In this case, control winding is supplied by voltage with variable amplitude value and shifted in phase by 90° relative to excitation voltage. The second method is phase control, where control winding is powered by voltage with constant amplitude. In this case, servomotor is controlled by changing the phase of that voltage. The third method is based on amplitude-phase control. In this case, both control voltage amplitude and its phase compared to excitation voltage are variable values.

Phase shift between current in starter winding and current in main winding is acquired by connecting starter winding in series with active or reactive resistance. The maximum value of starting torque is achieved by connecting starter winding in series with capacitor. However, since capacitor has considerable mass and volume, it negatively affects the use of servomotor with the control method.

Induction servomotors can be designed using the following rotor constructions: 1) squirrel cage rotor; 2) hollow non-magnetic rotor and 3) hollow ferromagnetic rotor. Design of single-phase servomotors with squirrel cage rotor is similar to a three-phase motor. The main single-phase winding of such an induction motor is placed in stator slots, while rotor is the same as squirrel cage rotor of a three-phase induction motor.

Servomotor with hollow non-magnetic rotor is designed with both inner and outer stators and rotor that is placed between them. Rotor of such a motor is designed as a hollow cylinder with thin walls and made of aluminum alloy. Servomotor with hollow ferromagnetic rotor has no inner stator because its rotor can conduct magnetic flux itself.

Servomotors with a hollow non-magnetic rotor have low mechanical inertia and thus have fast control reaction. However, a non-magnetic gap between inner and outer rotor is quite high, which leads to a decrease in efficiency and power coefficient as well as to an increase in mass and volume.

Single-phase induction motors have poor technical characteristics: significantly lower efficiency and power factor, lower overload ability, higher price compared to three-phase induction motors of the same power.

In order to ensure stable position according to the control signal, induction servomotors can be made using rotor with high active resistance, which leads to a further decrease in efficiency of the motor. Moreover, characteristics of induction servomotors are not linear.

Considering all problems mentioned above, it is important to study possibilities and features of the operation of synchronous electronically commutated motors in servomotor modes.

3. CONTROL OF ELECTRONICALLY COMMUTATED SYNCHRONOUS SERVOMOTORS

Synchronous permanent magnet motors and synchronous reluctance motors with electronic commutation are the objects of the present research. In general, rotation speed of these motors can be controlled by changing supply voltage for armature windings, which is somewhat similar to amplitude-control method of single-phase induction motors or armature control method of brushed DC motors. This task can also be achieved by changing angle θ (angle between vectors of the supply voltage and non-load electromotive force) or angle ε (angle between rotor direct axis and armature magnetomotive force axis).

The main electromagnetic parameters of brushless synchronous electronically commutated motors can be calculated using equations given in the present paper.

If the synchronous permanent magnet motor operates with control of angle θ , all basic electromagnetic parameters can be obtained from the following equations:

$$I_1 = \sqrt{\frac{U^2 - 2UI_2\omega L \cos \theta + \omega^2 I_2^2 L^2}{r_1^2 + \sigma^2 \omega^2 L^2}}, \quad (1)$$

$$T = \frac{mpI_2L}{r_1^2 + \sigma^2\omega^2L^2} [U(\sigma\omega L \sin \theta + r_1 \cos \theta) - I_2\omega Lr_1], \quad (2)$$

$$P_{em} = mI_2\omega L \left[\frac{U(\sigma\omega L \sin \theta + r_1 \cos \theta) - I_2\omega Lr_1}{r_1^2 + \sigma^2\omega^2L^2} \right], \quad (3)$$

$$\tan \varphi = \frac{\omega L [\sigma U - I_2(\sigma\omega L \cos \theta + r_1 \sin \theta)]}{Ur_1 + I_2\omega L(\sigma\omega L \sin \theta - r_1 \cos \theta)}, \quad (4)$$

and with control of angle ε all basic electromagnetic parameters can be obtained from the following equations:

$$I_1 = \frac{-I_2\omega L(\sigma\omega L \cos \varepsilon + r_1 \sin \varepsilon)}{r_1^2 + \sigma^2\omega^2L^2} + \frac{\sqrt{I_2^2\omega^2L^2(r_1 \sin \varepsilon + \sigma\omega L \cos \varepsilon)^2 + (r_1^2 + \sigma^2\omega^2L^2)(U^2 - I_2^2\omega^2L^2)}}{r_1^2 + \sigma^2\omega^2L^2}, \quad (5)$$

$$T = mpLI_1I_2 \sin \varepsilon, \quad (6)$$

$$P_{em} = m\omega LI_1I_2 \sin \varepsilon, \quad (7)$$

$$\tan \varphi = \frac{\omega L(\sigma I_1 + I_2 \cos \varepsilon)}{I_2\omega L \sin \varepsilon + I_1r_1}, \quad (8)$$

where ω is the armature current angular frequency proportional to the rotor rotational speed $n = \frac{\omega}{2\pi p}$;

- p is the number of pole pairs;
- m is the number of phases;
- L is the inductance corresponding to the flux of armature reaction;
- r_1 is the active resistance of the armature winding;
- I_2 is the current of the excitation winding reduced to the armature winding;
- I_1 is the current of the armature winding;
- T is the electromagnetic torque of the motor;
- P_{em} is the electromagnetic power of the motor;
- U is the phase voltage applied to the armature winding;
- φ is the phase shift angle between the armature voltage and current;
- σ is the dissipation factor of the armature winding.

Equations (1)–(8) have been obtained for a synchronous machine with non-salient poles. As known, the motors with permanent magnets have no excitation winding. Therefore, excitation current I_2 in these equations is calculated as equivalent, i.e., providing the same magnetic flux in the motor as obtained owing to perma-

nent magnets. The methodology for determination of this equivalent current for the synchronous permanent-magnet motor is given in [11].

If the synchronous reluctance motor operates with control of angle θ , the following equations describe motor electromagnetic parameters:

$$I_1 = \frac{U \sqrt{(\omega L_{ad} \sigma \sin \theta + r_1 \cos \theta)^2 + \left[\omega L_{ad} \left(\frac{k_q}{k_d} + \sigma - 1 \right) \cos \theta - r_1 \sin \theta \right]^2}}{r_1^2 + \sigma \omega^2 L_{ad}^2 \left(\frac{k_q}{k_d} + \sigma - 1 \right)}, \quad (9)$$

$$T = mpL_{ad}U_1^2 \times \frac{\left[\omega L_{ad} \left(\frac{k_q}{k_d} + \sigma - 1 \right) \cos \theta - r_1 \sin \theta \right] (\sigma \omega L_{ad} \sin \theta + r_1 \cos \theta) \left(1 - \frac{k_q}{k_d} \right)}{\left[r_1^2 + \sigma \omega^2 L_{ad}^2 \left(\frac{k_q}{k_d} + \sigma - 1 \right) \right]^2}, \quad (10)$$

$$P_{em} = \frac{m \omega L_{ad} U^2 \left[\omega L_{ad} \left(\frac{k_q}{k_d} + \sigma - 1 \right) \cos \theta - r_1 \sin \theta \right] (\sigma \omega L_{ad} \sin \theta + r_1 \cos \theta) \left(1 - \frac{k_q}{k_d} \right)}{\left[r_1^2 + \sigma \omega^2 L_{ad}^2 \left(\frac{k_q}{k_d} + \sigma - 1 \right) \right]^2}, \quad (11)$$

$$\text{tg} \varphi = \frac{\omega L_{ad} \left[\sigma \sin^2 \theta + \left(\frac{k_q}{k_d} + \sigma - 1 \right) \cos^2 \theta \right]}{r_1 + \frac{1}{2} \omega L_{ad} \left(1 - \frac{k_q}{k_d} \right) \sin 2\theta} \quad (12)$$

and with control of angle ε , the following equations describe motor electromagnetic parameters:

$$I_1 = \frac{U}{\sqrt{(\omega L_{ad} \sigma \cos \varepsilon + r_1 \sin \varepsilon)^2 + \left[\omega L_{ad} \left(\sigma - 1 + \frac{k_q}{k_d} \right) \sin \varepsilon - r_1 \cos \varepsilon \right]^2}}, \quad (13)$$

$$T = \frac{1}{2} mpL_{ad} I_1^2 \left(1 - \frac{k_q}{k_d} \right) \sin 2\varepsilon, \quad (14)$$

$$P_{em} = \frac{1}{2} m \omega L_{ad} I_1^2 \left(1 - \frac{k_q}{k_d} \right) \sin 2\varepsilon, \quad (15)$$

$$\operatorname{tg} \varphi = \frac{\omega L_{ad} \left(\cos^2 \varepsilon + \frac{k_q}{k_d} \sin^2 \varepsilon + \sigma - 1 \right)}{r_1 + \frac{1}{2} \omega L_{ad} \left(1 - \frac{k_q}{k_d} \right) \sin 2\varepsilon}. \quad (16)$$

where L_{ad} is the inductance that corresponds to the armature magnetic flux along the direct axis.

4. MECHANICAL AND CONTROL CHARACTERISTICS

Equations described in Section 3 allow calculating mechanical and control characteristics for synchronous motors and assessing their compatibility to servomotor requirements.

Figure 1 presents the calculated mechanical curves for synchronous permanent magnet motor with the following parameters: $p = 2$, $m = 3$, $U = 92$ V, $L = 0.00061$ H, $r_1 = 0.25$ Ω , $\sigma = 1.04$; equivalent excitation current $I_2 = 50$ A. The case with predetermined angle ε has mechanical curves with better linearity. All curves are given in relative values, where maximum value is taken as the base value.

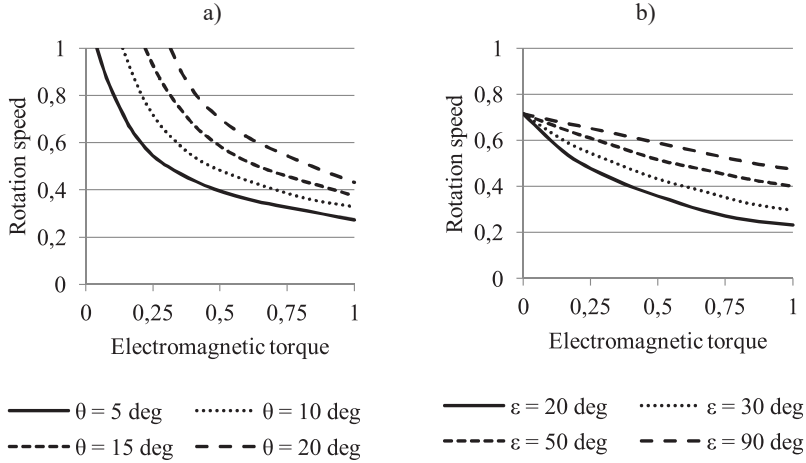


Fig. 1. Mechanical curves for permanent magnet synchronous motor with controlled angle θ (a) and controlled angle ε (b).

In the case of synchronous reluctance motor, the both mechanical curves with controlled angles θ and ε have similar form. As an example, mechanical curves with controlled angle ε are shown in Fig. 2. Parameters of synchronous reluctance motor are: $p = 1$; $m = 3$; $L_{ad} = 0.32$ H; $r_1 = 4.98$ Ω ; $\sigma = 1.15$; $k_q/k_d = 0.15$; $U = 220$ V.

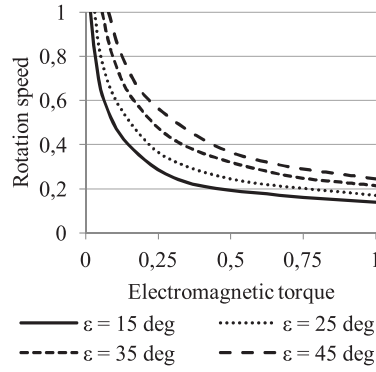


Fig. 2. Mechanical curves for synchronous reluctance motor with controlled angle ε .

Figure 3 demonstrates control curves for synchronous permanent magnet motor with variable supply voltage as operation mode with controlled voltage U , predetermined torque values and constant angles θ and ε . Permanent magnet motor control curves with variable supply voltage have similar form. Curve inclination angle depends on selected angle θ or ε values. A similar situation arises in case with a synchronous reluctance motor. For example, control curves for a synchronous reluctance motor with variable supply voltage with predetermined torque values and constant angle $\varepsilon = 45^\circ$ are shown in Fig. 4. Summarising the information, it is clear that the both synchronous motor types have similar control curves with variable supply voltage, which are close to linear.

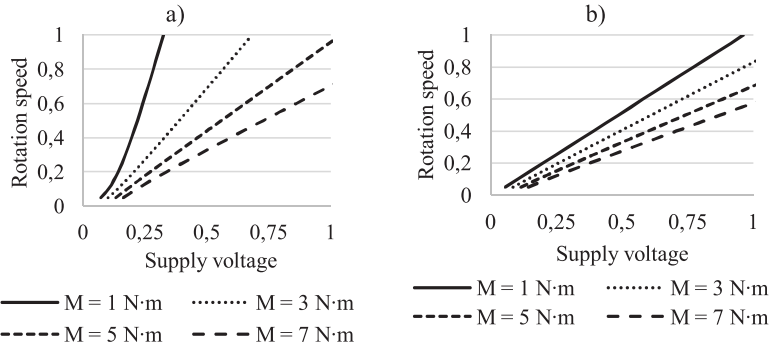


Fig. 3. Control curves for permanent magnet synchronous motor with variable supply voltage and constant angle $\theta = 30^\circ$ (a) and $\varepsilon = 45^\circ$ (b).

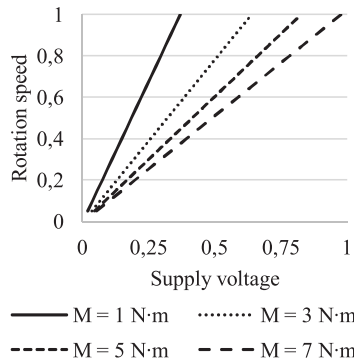


Fig. 4. Control curves for synchronous reluctance motor with variable supply voltage and constant angle $\varepsilon = 45^\circ$.

In order to operate the synchronous reluctance motor in servomotor modes, its rotation speed can be controlled by angle θ or ε , thus executing a specific phase control method. Control curves for permanent magnet synchronous motor with variable angle θ or ε are shown in Fig. 5, and for synchronous reluctance motor – in Fig. 6. Results show that in the case with angle θ as a control signal, curve form is more linear than in the case with control angle ε .

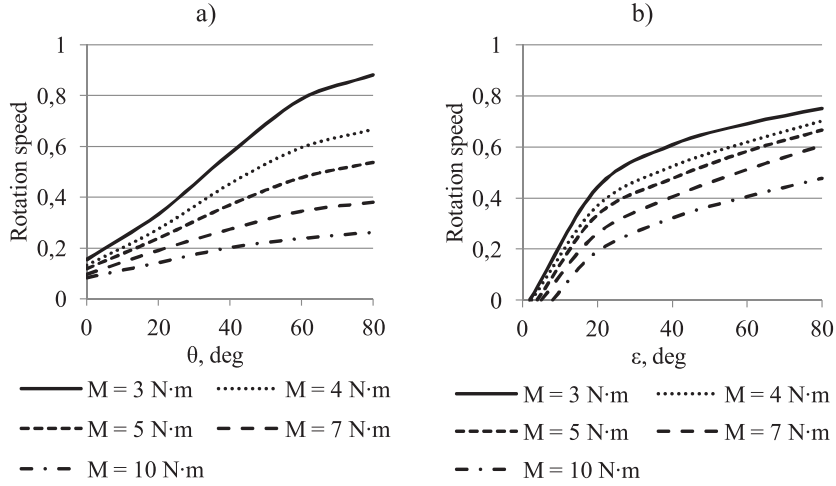


Fig. 5. Control curves $n = f(\theta)$ (a) and $n = f(\varepsilon)$ (b) for permanent magnet synchronous motor at $U = 92V$.

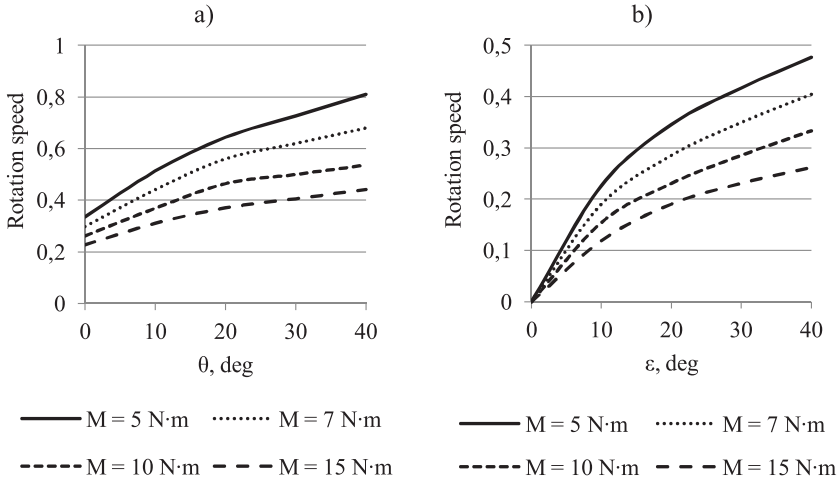


Fig. 6. Control curves $n = f(\theta)$ (a) and $n = f(\varepsilon)$ (b) for synchronous reluctance motor at $U = 220V$.

In order to prove the obtained results, theoretically calculated results, which are presented in this paper for synchronous reluctance motor, are compared with experimental results that are presented in the study [12] (Fig. 7). The experimental curve of the studied motor shows a good coincidence with the calculated curve.

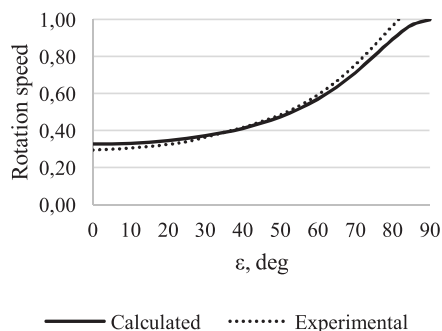


Fig. 7. Control curves for a synchronous reluctance motor.

5. CONCLUSIONS

Based on the results obtained, the following conclusions can be made:

1. Control of electronically commutated synchronous motors in servomotor operation modes can be achieved by the variation of angle θ (angle between vectors of the supply voltage and non-load electromotive force) or angle ε (angle between rotor direct axis and armature magnetomotive force axis).
2. Mechanical characteristics of a synchronous permanent magnet motor are more linear in comparison with the corresponding characteristics of a synchronous reluctance motor.
3. Synchronous electronically commutated motors as servomotors have sufficient potential as an alternative to DC and AC servomotors.

ACKNOWLEDGEMENTS

The present research has been supported by the State Research Programme “LATENERGI”.

REFERENCES

1. Huges, A. (2006). *Electric Motors and Drives. Fundamentals, Types and Applications* (3rd ed.). Newnes. ISBN-13: 978-0-7506-47182.
2. Firoozian, R. (2014). *Servo Motors and Industrial Control Theory* (2nd ed). Springer. ISBN-13: 978-3319072746.
3. Wahyunggoro, O., & Saad, N. (2010). Analysis and evaluation of real-time and s-domain model of a DC servomotor. In *Intelligent and Advanced Systems (ICIAS)*, 2010 International Conference (pp. 1–5). DOI: 10.1109/ICIAS.2010.5716206.
4. Levin, N., Kamolins, E., & Vitolina, S. (2014). *Brushless Electric Machines*. Riga: RTU (in Latvian).

5. Dote, Y., & Kinoshita, S. (1990). *Brushless Servomotors Fundamentals and Applications*. Oxford: Clarendon Press.
6. Zorlu, S., Senol, I., & Bakan, A.F. (2006). Vector control of an AC brushless servomotor using a custom-designed motion control card. In *2006 IEEE International Symposium on Industrial Electronics* (vol. 3, pp. 2516–2521). DOI: 10.1109/ISIE.2006.295968.
7. Terentiev, S.A., Povernov, E.S., & Sypin, E.V. (2004). The direct-current servomotor control system. In *Proceedings of the 5th Annual International Siberian Workshop on Electron Devices and Materials* (pp. 184–186). DOI: 10.1109/PESC.2004.241338.
8. Pillay, P., & Krishnan, R. (1991). Application characteristics of permanent magnet synchronous and brushless DC motors for servo drives. *IEEE Transactions on Industry Applications*, 27(5), 986–996. DOI: 10.1109/28.90357.
9. Dirba, J., Lavrinovicha, L., & Dobriyan, R. (2015). The prospects of synchronous reluctance motors usage in low power electrical devices. *Latv. J. Phys. Tech. Sci.*, 52(2), 40–48. DOI: 10.1515/lpts-2015-0010.
10. Lavrinovicha, L., & Dirba, J. (2015). *Brushless Synchronous Motors with External Rotor*. Riga: RTU (in Latvian).
11. Dirba, J., Roldugina, N., & Pugačevs, V. (2001). Methodology of permanent magnet brushless DC motor calculation and optimization. *Scientific Proceedings of Riga Technical University: Power and Electrical Engineering* (Ser. 4, Vol 4, pp. 48–53) (in Latvian).
12. Dirba, J. (1997). *Special Operation Modes of Synchronous Machines*. Riga: RTU (in Latvian).

SINHRONO VENTIĻDZINĒJU DARBA ĪPATNĪBAS SERVODZINĒJU REŽĪMOS

J. Dirba, L. Lavrinoviča, R. Dobrijans

K o p s a v i l k u m s

Aplūkotas sinhrono ventiļdzinēju ar pastāvīgajiem magnētiem un sinhrono reaktīvo ventiļdzinēju iespējas un darbības īpatnības servodzinēju režīmos. Aprēķinātas to mehāniskās un regulēšanas raksturlielnes, kas ir tuvas lineārām. Piedāvāts minēto dzinēju vadību īstenot līdzīgi kā asinhroniem servodzinējiem ar fāžu vadību, t. i. mainot leņķi θ starp dzinēja pret EDS un barošanas sprieguma vektoriem vai leņķi ϵ starp enkura magnetodzinējspēka asi un rotora garenasi. Parādīts, ka sinhronos ventiļdzinējus daudzos gadījumos var izmantot kā servodzinējus.

10.05.2016.

ENVIRONMENTAL AND ENERGY ASPECTS OF
CONSTRUCTION INDUSTRY AND GREEN BUILDINGS

L.Kauskale¹, I. Geipele¹, N. Zeltins², I. Lecis¹

¹Riga Technical University,
Institute of Civil Engineering and Real Estate Economics,
6-210 Kalnciema Str., LV-1048, Riga, LATVIA

e-mail: Linda.Kauskale@rtu.lv

²Institute of Physical Energetics
11 Krivu Str. Riga, LV-1006, LATVIA

Green building is an important component of sustainable real estate market development, and one of the reasons is that the construction industry consumes a high amount of resources. Energy consumption of construction industry results in greenhouse gas emissions, so green buildings, energy systems, building technologies and other aspects play an important role in sustainable development of real estate market, construction and environmental development. The aim of the research is to analyse environmental aspects of sustainable real estate market development, focusing on importance of green buildings at the industry level and related energy aspects. Literature review, historical, statistical data analysis and logical access methods have been used in the research. The conducted research resulted in high environmental rationale and importance of environment-friendly buildings, and there are many green building benefits during the building life cycle. Future research direction is environmental information process and its models.

Keywords: *construction, energy efficiency, environment, sustainable real estate market development.*

1. INTRODUCTION

The reduction of greenhouse gas emissions is one of the most important environmental priorities globally, and sustainable real estate market development can result in reduction of greenhouse gas emissions as well.

The aim of the research is to analyse environmental aspects of construction and sustainable real estate market development, focusing on importance of green buildings at the industry level and related energy aspects. Literature review, historical, statistical data analysis and logical access methods have been used in the research. Practical part focuses on the case study of Europe and comparison of environmental development tendencies between Germany and Latvia. The **object of the**

research is environmental development tendencies. *The subject of the research* is green building environmental and energy issues. The research comprises experience of the European Union, including case of Latvia and Germany.

Growing attention to environmental protection has changed the corporate practices of construction firms, for example, several studies have shown that some multinational companies have been proactive in environmental management; however, the financial outcomes of environmental practices have not been fully comprehended [1]. The same research suggests that careful distinction needs to be made between the benefits that are planned to be experienced by the company, but for the evaluation of the environmental impacts created by buildings, it is necessary to adopt a life cycle analysis (LCA).

Concepts of sustainability have been described earlier in previous studies [2], [3]. The present research focuses on environmental aspects of real estate market sustainability. The present research is the continuation of previously conducted research on energy aspects in green buildings [4]. An analysis of technical aspects of green buildings has shown a number of opportunities during the building life cycle.

2. OVERVIEW OF THEORETICAL ASPECTS

At present, green building construction is considered to be an essential practice for achieving sustainability [5]. As defined in previous studies, “real estate market sustainability is a concept that includes economic, social, environmental, political, technological and legal aspects of real estate market development, long-term national and real estate market development policies that include equity principles, conservation and preservation of the environment and improve the quality of life of society” [3].

Construction industry is one of the largest final consumers of environmental resources and one of the largest emitters of greenhouse gases and other types of pollution, but before the 21st century, for instance, in China, green building construction has not received much attention [6].

Environmental aspects of real estate market sustainability are of high social and economic importance. Diverging interests and needs with the choice of construction and social goals are:

- Planning effort for financial commitment;
- Energy saving and financial gain;
- Reduction of CO₂ and environmental management;
- Use of chemicals and possible pollutants in the production of products [7, p.156].

Green buildings are of special importance in sustainable real estate market development and have environmental, social and economic benefits during the object life cycle for stakeholders and market participants. Building materials also play a significant role in green building costs and energy efficiency aspects.

“A green building material (GBM) is an ecological, health-promoting, recycled, or high-performance building material that impacts the material selection to cover all

three pillars (3Ps) of sustainability” [8, p.1]. The potential of green building materials based on the three sustainability criteria is shown in Table 1.

Table 1

Potential of GBMs Based on Three Sustainability Criteria [9, p. 3]

Criteria	Benefit
Environmental benefits	Enhancing and protecting ecosystems; improving air and water quality; decreasing waste streams to air and land; preserving and restoring natural and renewable resources
Economic benefits	Decreasing operating costs; creating, expanding, and shaping markets for green products and services; improving occupant productivity; and optimising life-cycle economic performance
Social benefits	Enhancing occupant comfort and health; heightening aesthetic qualities; minimising strain on local infrastructure; and improving overall quality of life

Green buildings include a variety of necessary aspects for sustainable development of construction industry, as well as environment and society. Green buildings can be defined as follows:

“Green building is the practice of creating structures and using processes that are environmentally responsible and resource-efficient throughout a building’s life-cycle from siting to design, construction, operation, maintenance, renovation and deconstruction. This practice expands and complements the classical building design concerns of economy, utility, durability, and comfort. Green building is also known as a sustainable or high performance building.” [10].

“A green building focuses on increasing the efficiency of resource use – energy, water, and materials – while reducing building impact on human health and the environment during the building’s lifecycle, through better siting, design, construction, operation, maintenance, and removal. Green buildings should be designed and operated to reduce the overall impact of the built environment on its surroundings.” [11].

“Green building is a holistic concept that starts with the understanding that the built environment can have profound effects, both positive and negative, on the natural environment, as well as the people who inhabit buildings every day. Green building is an effort to amplify the positive and mitigate the negative of these effects throughout the entire life cycle of a building.”. [12].

“Green building is a comprehensive process of design and construction that employs techniques to minimise adverse environmental impacts and reduce the energy consumption of a building, while contributing to the health and productivity of its occupants.” [13].

Green building assessment often includes life cycle assessment as well. Methods and concepts of life cycle assessment include the following aspects: cumulative energy expenditure, carbon footprint, virtual water, environmental impact points, MIPS (material intensity per service unit), Eco-Indicator 99, Critical Volumes, ABC Analysis and other methods [14].

Comfort can be influenced by many factors. Indoor comfort factors are shown in Fig. 1.

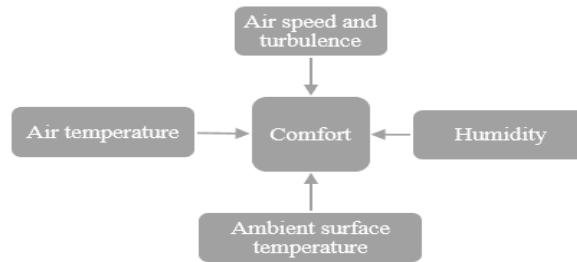


Fig. 1. Comfort factors [7, p.51].

Health aspects are very important in green buildings. According to the research that examined 30 participants in green buildings and conventional buildings for two weeks [6], participants in green buildings experienced significantly lower CO₂ concentrations, reports of too little air flow were reduced by 91 %, chemical odours by 22 %, tobacco smoke odours by 88 %, other unpleasant odours by 28 %, dryness by 63 %, and the participants in green buildings reported half as many symptoms per day as those in the conventional buildings – eye and skin, cognitive, viral, and sensory symptoms were reduced by 67 %, 70 %, 28 %, 50 % and 65 %, respectively. As a result, green buildings have lower environmental impacts and improve health and well-being of occupants, by such improvements as ventilation, lighting, materials, and improved indoor environmental quality.

To evaluate design alternatives for economic and environmental criteria, the life cycle assessment methodology can be employed, including the analysis of expanded cumulative exergy consumption that often needs effective systems to recover the negative impacts of waste emissions [15]. Life cycle analysis is crucial for analysis of building impact on environment as well because it includes energy aspects. The general distributive sustainability related to the overall greenhouse gases per capita seems to decrease since 2000; however, the analysis of different gases also indicates some differences in temporal variations and depending on the index used [16]. “Life cycle assessment (LCA) is a system analysis method that is useful in understanding and evaluating the resource consumption and waste emissions associated with products, processes and activities, across all phases of their life cycle from materials acquisition to final disposition” [17]. In the analysis, special attention is devoted to ESG (economic, social and governance) criteria, and in the infrastructure analysis the following criteria are also taken into account [18, p. 5]:

- Diversification at the group level;
- Waste treatment and disposal;
- Water resource management;
- Telecommunications;
- Energy transmission and distribution;
- Energy efficiency;
- Energy generation;
- Transportation;
- Social;
- Other.

Grey energy and share of primary energy expenditure in the object life cycle should be analysed in the following categories of pre-processes, such as raw material production, production, transport, storage, sales, and post-processes – disposal and demolition / dismantling [7, p. 96]. Energy sources for the calculation of grey energy are shown in Table 2.

Table 2

Energy Sources for the Calculation of Grey Energy [19, p.96]

Recognised energy carriers	Unrecognised energy carriers
Petroleum, natural gas, coal and all fuel and raw materials derived from energy value as a result of combustion	Wood, cork and other vegetable and animal raw materials, as well as energy carriers derived from sustainable management
Natural uranium with the heat usable in light water reactors	Solar energy, geothermal energy, wind energy, ambient heat and all secondary energy forms
Hydroelectric power with the mechanical energy that can be used on the turbine blade	Plastic waste, waste paper, used tires, sewage sludge, and other waste recycled materially or energetically

Integration of sustainability aspects in the building also gives high technical benefits. Green building environmental benefits are the following [20]:

- Emissions Reduction. Pollutants released by fossil fuel contribute to global climate change, cause air quality issues, such as acid rain and smog, and pose risks to human health [2]. Green building techniques like solar powering, daylighting, and facilitation of public transport increase energy efficiency and reduce harmful emissions.
- Water Conservation. Recycling rainwater and greywater for purposes such as urinal flow and irrigation can preserve potable water and yield significant water savings.
- Stormwater Management. Stormwater runoff can cause waterway erosion, flooding, and carry pollutants into water sources. Harvesting and redirecting storm water, building surfaces with permeable materials, and using green roofs can control and utilise overflow.
- Temperature Moderation. The heat retention properties of tall buildings and urban materials, such as concrete and asphalt, are the primary causes of urban heat island effect. These conditions may be offset by conscientious building design and site selection, as well as planting trees to accompany new developments.
- Waste Reduction. Construction and demolition generates a huge portion of solid waste in the United States. Building deconstruction as an alternative to full-scale demolition results in massive decreases of waste production [15].

Using Germany as an example, just Big Seven locations (Berlin, Dusseldorf, Frankfurt, Hamburg, Cologne, Munich, Stuttgart) have the market share of over 80 %, and the unique leader is Munich, where over one billion EUR was invested in certified buildings, followed by Hamburg, Berlin and Frankfurt [21]. The main investors in 2014 were open funds (47.8 %), insurance companies (37.1 %), state funds (35.3 %), pension funds (28.4 %) and equity/ real estate funds (24.1 %) [21].

There are many positive environmental aspects of green buildings. At present, investment tendencies are positive in green buildings, and the number of certified green buildings increases.

3. ENVIRONMENTAL AND ENERGY ASPECTS OF CONSTRUCTION

Green building activities could help achieve energy efficiency and renewable energy aims. Major greenhouse gases (CO_2 , CH_4 , N_2O) and two acidic gases (SO_x and NO_x) negatively affect the environment [15]. Figure 2 demonstrates carbon dioxide emissions from all NACE activities in Germany and Latvia in period from 2008 to 2012.

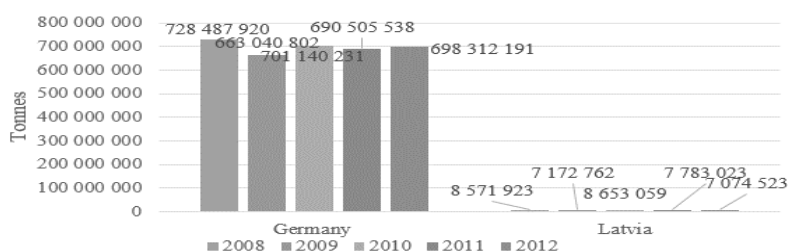


Fig. 2. Carbon dioxide emissions – all NACE activities from 2008 to 2012 [22].
[Figure made by the authors]

Size of market is of high importance in carbon dioxide emissions. Influence of the construction sector on environmental development can show share of carbon dioxide air emissions of construction industry to total emissions (Fig. 3.).

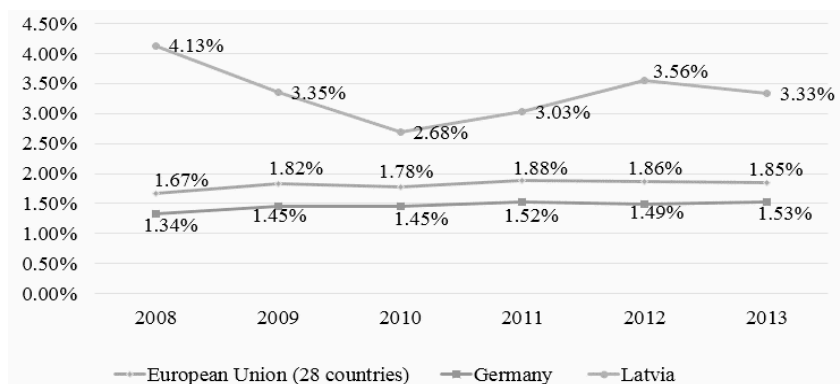


Fig. 3. Share of carbon dioxide air emissions of construction industry to total emissions, %.
Data: Eurostat [22]. [Figure made by the authors]

Share of carbon dioxide air emissions of construction industry to total emissions in Latvia is higher than an average EU indicator, which is not a positive tendency. Indicator of Germany is lower than an average indicator in 28 member states of the European Union (EU-28). Data analysis of primary and final energy consumption is also important. Table 3 demonstrates primary and final energy consumption in million tonnes of oil equivalent from 2000 to 2014 in EU, Germany and Latvia.

Table 3

Primary and Final Energy Consumption, Million TOE (Tonnes of Oil Equivalent).
Data: Eurostat [22]. Last update 04/02/2016 [Table made by the authors]

GEO/ TIME		EU-28	Germany	Latvia		EU-28	Germany	Latvia
2000	Primary energy consumption	1 617.9	317.3	3.8	Final energy consumption	1 132.8	220.0	3.3
2001		1 658.2	327.3	4.1		1 156.5	223.6	3.6
2002		1 653.4	319.7	4.0		1 144.6	220.1	3.6
2003		1 690.5	318.3	4.3		1 176.3	223.5	3.8
2004		1 708.5	320.1	4.4		1 188.9	221.6	3.9
2005		1 712.8	317.2	4.5		1 191.8	218.5	4.0
2006		1 722.0	327.6	4.7		1 193.0	223.4	4.2
2007		1 693.6	310.4	4.8		1 172.9	210.2	4.4
2008		1 693.1	315.2	4.6		1 180.0	217.6	4.2
2009		1 599.4	296.0	4.4		1 114.7	205.8	4.0
2010		1 656.4	310.4	4.6		1 163.3	219.7	4.1
2011		1 593.3	294.4	4.3		1 105.0	208.8	3.9
2012		1 584.0	296.8	4.4		1 104.5	212.1	4.0
2013		1 569.1	302.8	4.4		1 106.2	217.7	3.9
2014		1 507.1	291.8	4.4		1 061.2	208.9	3.9

In Latvia, primary and final energy consumption is increasing, but in Germany and the European Union in general – the decreasing tendencies are observed. Economic aspect of the used energy results in energy prices. Tables 4 and 5 show energy price tendencies for gas and electricity for domestic and industrial consumers in Germany and Latvia in 2016S1.

Table 4

Gas Prices for Consumers – Bi-annual Data, All Taxes and Levies Included, in 2016S1, Unit Kilowatt-Hour, in Euro [22]. [Table made by the authors]

GEO/TIME	Germany	Latvia
Gas prices for domestic consumers		
Band D1 : Consumption < 20 GJ	0.1091	0.0698
Band D2 : 20 GJ < Consumption < 200 GJ	0.0661	0.0424
Band D3 : Consumption > 200 GJ	0.0610	0.0424
Gas prices for industrial consumers		
Band I1 : Consumption < 1 000 GJ	0.0539	0.0406
Band I2 : 1 000 GJ < Consumption < 10 000 GJ	0.0423	0.0364
Band I3 : 10 000 GJ < Consumption < 100 000 GJ	0.0404	0.0323
Band I4 : 100 000 GJ < Consumption < 1 000 000 GJ	0.0316	0.0301
Band I5 : 1 000 000 GJ < Consumption < 4 000 000 GJ	0.0264	0.0291
Band I6 : Consumption > 4 000 000 GJ	0.0246	:

Table 5

Electricity Prices for Domestic and Industrial Consumers, Bi-annual Data, all Taxes and Levies Included, Unit Kilowatt-Hour, in Euro [22]. [Table made by the authors]

GEO/TIME	Germany	Latvia
Electricity prices for domestic consumers		
Band DA : Consumption < 1 000 kWh	0.4555	0.1614
Band DB : 1 000 kWh < Consumption < 2 500 kWh	0.3263	0.1630
Band DC : 2 500 kWh < Consumption < 5 000 kWh	0.2969	0.1628
Band DD : 5 000 kWh < Consumption < 15 000 kWh	0.2812	0.1619
Band DE : Consumption > 15 000 kWh	0.2680	0.1583
Electricity prices for industrial consumers		
Band IA : Consumption < 20 MWh	0.2804	0.1852
Band IB : 20 MWh < Consumption < 500 MWh	0.2259	0.1555
Band IC : 500 MWh < Consumption < 2 000 MWh	0.1974	0.1410
Band ID : 2 000 MWh < Consumption < 20 000 MWh	0.1712	0.1300
Band IE : 20 000 MWh < Consumption < 70 000 MWh	0.1398	0.1211
Band IF : 70 000 MWh < Consumption < 150 000 MWh	0.1130	0.0946
Band IG : Consumption > 150 000 MWh	-	-

Energy prices differ by consumer groups; however, energy prices for all groups are important for the development of all sectors of national economy. Example of the construction industry shows that sustainable development of construction industry plays an important role in the balanced environmental development.

4. RESULTS AND DISCUSSION

The research results have shown that there is a need for green building construction, but at the same time there are a number of risks and conflicting criteria during its implementation. As sustainable development includes also social and economic factors, an optimal balance should be found by market participants. Investment tendencies to green buildings are also of special importance, as financial aspects and information are one of the important factors for construction of green buildings.

5. CONCLUSIONS

1. The construction industry exerts a great influence on environmental development, and green buildings include a variety of positive aspects and parameters for sustainable development of construction industry.
2. Consumption of energy is of high environmental importance, and at the same time energy prices play an important socio-economic role. Energy consumption volumes are the criteria that affect energy prices, and each country has a particular structure of companies by size and other criteria. Energy efficiency policies should differ among different sectors of real estate (and its subsectors) by type of activities, different groups of society, etc.
3. Share of carbon dioxide emissions in Latvia is much lower in comparison with Germany due to the size of market, but share of carbon dioxide emissions in the construction industry, in particular, is higher. The research results show that according to the analysed indicators, energy development tendencies in Germany

and Latvia differ. Implementation of effective energy policies in the construction industry can give positive results for environmental development in the long term for many market participants, i.e., they can influence the business sector – construction entrepreneurs and renters, households (consumers of energy during the building life cycle) and government buildings in the construction and maintenance period.

REFERENCES

1. Chen, P.-H., Ong, C.-F., & Hsu, S.-C. (2016). Understanding the relationships between environmental management practices and financial performances of multinational construction firms. *Journal of Cleaner Production*, 139, 750–760. <http://dx.doi.org/10.1016/j.jclepro.2016.08.109>
2. Kauškale, L., & Geipele, I. (2016). Economic and social sustainability of real estate market and problems of economic development – a historical overview. *Baltic Journal of Real Estate Economics and Construction Management*, 4(1), 2255–9671. DOI: 10.1515/bjreecm-2016-0002
3. Kauškale, L., & Geipele, I. (2017). Integrated approach of real estate market analysis in sustainable development context for decision making. *Procedia Engineering*, 172, 505–512. DOI:10.1016/j.proeng.2017.02.059
4. Kauškale, L., Geipele, I., Zeltiņš, N., & Lecis, I. (2016). Energy aspects of green buildings – international experience. *Latvian Journal of Physics and Technical Sciences*, 6, 21–28. DOI:10.1515/lpts-2016-0040
5. Vyas, G.S., & Jha, K.N. (2017). Benchmarking green building attributes to achieve cost effectiveness using a data envelopment analysis. *Sustainable Cities and Society*. 28, 127–134. <http://dx.doi.org/10.1016/j.scs.2016.08.028>
6. MacNaughton, P., Spengler, J., Vallarino, J., Santanam, S., Satish, U., & Allen, J. (2016). Environmental perceptions and health before and after relocation to a green building. *Building and Environment*, 104, 138–144. <http://dx.doi.org/10.1016/j.buildenv.2016.05.011>
7. Neddermann, R., & Weber, C. (2016). *Energetische Optimierung im Wohnungsbau. Wirtschaftlichkeit – Nutzen – Effizienz* [Energetic Optimization in Construction. Profitability – Usage – Efficiency]. Stuttgart: Fraunhofer IRB.
8. Khoshnava, S.M., Rostami, R., Valipour, A., Ismail, M., & Rahmat, A.R. (2016). Rank of green building material criteria based on the three pillars of sustainability using the hybrid multi criteria decision making method. *Journal of Cleaner Production*, 1–18. DOI: 10.1016/j.jclepro.2016.10.066
9. U.S. Environmental Protection Agency. (2009). *Municipal Solid Waste Generation, Recycling, and Disposal in the United States: Facts and Figures for 2008*. EPA-530-F-009-021. Washington, D.C. Retrieved 11 November 2016 from www.epa.gov/epawaste/nonhaz/municipal/pubs/msw2008rpt.pdf
10. US Environmental protection agency. *Green Building*. Retrieved 20 November 2016 from <https://archive.epa.gov/greenbuilding/web/html/>
11. Greenbuildingindex SDN BHD. *What is Green Building?* Retrieved 20 November 2016 from <http://new.greenbuildingindex.org/whatandwhy>
12. U.S. Green Building Council. *What is green building?* Retrieved 20 November 2016 from <http://www.usgbc.org/articles/what-green-building>
13. Smith College. Smith Sustainability News. *Glossary of Green Terms*. Retrieved 11 November 2016 from https://www.smith.edu/green/news_glossary.php
14. Springer Gabler Publishing House. *Gabler Wirtschaftslexikon* [Gabler Economic Lexicon]. Ökobilanz [Life Cycle Assessment]. Retrieved 11 November 2016 from <http://wirtschaftslexikon.gabler.de/Archiv/57090/oekobilanz-v13.html>

15. Wang, W., Zmeureanu, R., & Rivard, H. (2005). Applying multi-objective genetic algorithms in green building design optimization. *Building and Environment*, 40, 1512–1525. DOI:10.1016/j.buildenv.2004.11.017
16. Duro, J.A. (2016). Intercountry inequality on greenhouse gas emissions and world levels: An integrated analysis through general distributive sustainability indexes. *Ecological Indicators*, 66, 173–179. <http://dx.doi.org/10.1016/j.ecolind.2016.01.026>
17. Barnthouse, L., Fava, J., Humphreys, K., Hunt, R., Laibson, L., Noesen, S., Norris, G., Owens, J., Todd, J., Vigon, B., Weitz, K., & Young, J. (2005). *Life Cycle Impact Assessment: The State-of-the-Art* (2nd ed). Pensacola, FL: SETAC Press 1998, as cited in W. Wang, R. Zmeureanu, & H. Rivard (2005). Applying multi-objective genetic algorithms in green building design optimization. *Building and Environment*, 40, 1512–1525. DOI:10.1016/j.buildenv.2004.11.017
18. GRESB B.V. *Infrastructure*. 2016 Report. Retrieved 20 November 2016 from https://gresb-public.s3.amazonaws.com/2016/content/2016_Infrastructure_Report.pdf
19. WECOBIS Bundesministerium für Umwelt, Naturschutz, Bau und Reaktorsicherheit [Federal Ministry for the Environment, Nature Conservation, Construction and Nuclear Safety, German Federation] and Bayerischen Architektenkammer (ByAK) [Bavarian Chamber of Architects (ByAK)]. (2016). *Energy Sources for the Calculation of Grey Energy* as cited in T. Duzia, & R. Mucha (2016). *Energetisch optimiertes Bauen: technische Vereinfachung - nachhaltige Materialien - wirtschaftliche Bauweisen* [Energetically optimized construction: technical simplification - sustainable materials - economical construction]. Stuttgart: Fraunhofer.
20. National Association of Home Builders. (1998). *Deconstruction: Building Disassembly and Material Salvage*, as cited in The City of Bloomington. Green Building benefits. Retrieved 10 November 2016 from <https://bloomington.in.gov/green-building-benefits>
21. BNP Paribas Real Estate. (2014). Market Focus. *Investmentmarkt green Buildings 2014* [Market Focus. Investment market of green buildings]. Retrieved 20 January 2017 from https://www.realestate.bnpparibas.de/upload/docs/application/pdf/2016-05/2014-q4_green_building_investment_de_final.pdf?id=p_1626804&hreflang=de
22. *European Statistics Database Eurostat. Statistics Database*. Retrieved 20 November 2016 from <http://ec.europa.eu/eurostat/data/database>

BŪVNICĪBAS NOZARES VIDES UN ENERĢĒTIKAS ASPEKTI, UN ZAĻĀ BŪVNICĪBA

L.Kauškale, I.Geipele, N.Zeltiņš, I.Lecis

K o p s a v i l k u m s

Zaļā būvniecība ir svarīga ilgtspējīgas būvniecības nozares un nekustamā īpašuma tirgus attīstības daļa, kas saistīta ar būvniecības nozarei raksturīgo lielo resursu patēriņu. Būvniecības nozares darbības rezultātā enerģijas patēriņš rada siltumnīcefekta gāzu emisijas, tāpēc zaļai būvniecībai, enerģijas sistēmām, ilgtspējīgām būvniecības tehnoloģijām, energoresursu cenām un citiem svarīgiem jautājumiem ir būtiska nozīme ilgtspējīgā būvniecības nozares un nekustamā īpašuma tirgus attīstībā, un kopējai vides attīstībai valstī. Veiktā pētījuma rezultāti atspoguļo augsto vides draudzīgas būvniecības ekoloģisko nozīmi. Pētījuma gaitā tiek analizētas dažādas zaļo ēku būvniecības priekšrocības ēku un būvju dzīves cikla laikā, un enerģijas resursu cenas.

06.02.2017.

NANOINDENTATION RESPONSE ANALYSIS OF THIN FILM
SUBSTRATES-II: STRAIN HARDENING-SOFTENING OSCILLATIONS IN
SUBSURFACE LAYERUldis Kandars¹, Karlis Kandars²¹Institute of Mechanical Engineering,

Riga Technical University,

6 Ezermalas Str., LV-1006, Riga, LATVIA

e-mail: uldis.kandars@gmail.com

²Institute of Neuroinformatics, University & ETH of Zurich

190 Winterthurerstr., CH-8057 Zurich, SWITZERLAND

e-mail: kkandars@ini.phys.ethz.ch

We have extracted stress-strain field (SSF) gradient and divergence representations from nanoindentation data sets of bulk solids often used as thin film substrates: bearing and tooling steels, silicon, glasses, and fused silica. Oscillations of the stress-strain field gradient and divergence induced in the subsurface layer by the nanoindentation have been revealed. The oscillations are especially prominent in single indentation tests at shallow penetration depths, $h < 100$ nm, whereas they are concealed in the averaged datasets of 10 and more single tests. The amplitude of the SSF divergence oscillations decays as a sublinear power-law when the indenter approaches deeper atomic layers, with an exponent -0.9 for the steel and -0.8 for the fused silica. The oscillations are interpreted as alternating strain hardening-softening plastic deformation cycles induced in the subsurface layer under the indenter load.

Keywords: *elastic-plastic deformation, heterogeneity, nanoindentation, strain gradient plasticity, stress-strain field, subsurface layer.*

1. INTRODUCTION

When bulk solids are used as substrates for deposition of thin and very thin films, a detailed understanding of the substrate surface and subsurface layers at depths of several hundred to thousand nanometers is a prerequisite for an adequate assessment of the deposited thin film mechanical properties. Nanoindentation is a convenient and versatile experimental technique used to characterise the mechanical properties of small volume samples, including subsurface layers of bulk solids, as well as thin films and coatings, or even biological materials like bone, tooth enamel and viruses [1]–[5]. The subsurface layer of bulk solids, especially of polished steel substrates, is, however, usually somewhat deformed and highly heterogeneous and

may not yield a steady state value of the apparent hardness and/or elastic modulus [3], [6] that would correspond to the so-called material bulk property. In this case, it would be valuable to probe the local gradients and inhomogeneities in a better detail to reveal more information about the microstructure of the sample subsurface layer.

In the first part of this investigation, we derived a simple approach to extract the local stress-strain field (SSF) gradient and divergence representations from the nanoindentation experiment dataset [7]. These representations, in principle, allow discovering weak structural heterogeneities which might point to, for example, interfaces between mechanically distinct local microzones within the subsurface region or work hardening and softening deformation processes induced underneath the indenter. Here, we applied the strain gradient-divergence approach [7] in the analysis of nanoindentation response of bulk solids commonly used as substrates for thin film deposition: different types of bearing and tooling steels, glass, silicon as well as silica as a reference sample without a pretreated surface. A highly dynamic process occurring in the subsurface layer of the bulk solids was revealed during a nanoindentation experiment: oscillations of the stress-strain field gradient and divergence. The gradient-divergence oscillations are best discernible in the single measurement data at shallow penetration depths below 100 nm, where the averaged measurement has the highest variability and thus is commonly discarded. We associate these oscillations with alternating cycles of strain hardening and strain softening processes of the elastic-plastic deformation induced during the indentation experiment. The terms *strain hardening* and *strain softening* are used here in a general sense, encompassing many possible underlying specific plastic deformation mechanisms such as slipping, twinning, serration, [8]–[10] etc. (as opposed to the restricted, historical meaning of the terms as processes caused by the dislocation creation and movement in crystal-line materials).

2. METHODS

2.1 Experimental Details

Various bulk samples of steel, glass, silicon, and fused silica substrates were tested in the nanoindentation experiments. The steel samples, labelled as 100Cr6 (OTAI Special Steel) and SCH (Schaeffler Technologies AG) were classified as bearing steel. The other category of steel samples labelled as CZS and HVG (ProfProkat) corresponded more to tooling steels. All of them were of high quality chrome low-alloy steels closely matching the AISI 52100 steel with minor modifications depending on their respective manufacturers. The glass sample was the hard glass microscope slide VB5 656. In turn, silicon substrates were Si(100) as thick as 0.5 mm cut off from high quality silicon wafer having root mean square (RMS) less 1 nm. Fused silica was the Corning HPFS 7980, Standard Grade high purity synthetic amorphous silicon dioxide.

Surface morphology, microstructure, phase structure and elemental composition of the samples were estimated by scanning electron microscope (model Hitachi S-4800) equipped with the energy dispersive spectrometer B-Quantax and X-ray fluorescence spectrometer S4 PIONEER. X-ray diffraction structure measurements were performed by Bruker D8 Advance.

Surface roughness RMS was measured by atomic force microscope (AFM, model Veeco CP-II and Asylum Research, model MFP-3D) in tapping mode. The surface micrographs and phase images were taken from surface area of 20 μm x 20 μm . Surface profiler Dektak 150 was used to probe surface texture and roughness over a wider area, on the order of millimeter. The Dektak 150 resolution features enabled precise planarity scans for measuring radius of curvature, flatness, and waviness.

Instrumented depth sensing nanoindentation experiments were performed by G200 Nano Indenter (Agilent, USA) with a sharp Berkovich diamond indenter (tip radius < 20 nm). Measurements were made in the continuous stiffness measurement (CSM) mode [11] and in the BASIC mode at different values of the maximum load. The load capability of the Nano Indenter G200 reaches up to 600 mN within the standard option. The hardness and elastic modulus of the samples were calculated using Oliver-Pharr method [12] by MTS TestWorks 4 software.

2.2. Stress-Strain Field Gradient and Divergence Representations

The specialized elastic-plastic strain gradients are extracted from the experimental load, $P(h)$, stiffness, $S(h)$, elastic modulus, $E(h)$, and hardness, $H(h)$, datasets by

$$\begin{aligned} P'(h) &\equiv \frac{h}{P(h)} \frac{dP(h)}{dh} - 2, \\ S'(h) &\equiv \frac{h}{S(h)} \frac{dS(h)}{dh} - 1, \\ E'(h) &\equiv \frac{h}{E(h)} \frac{dE(h)}{dh}, \\ H'(h) &\equiv \frac{h}{H(h)} \frac{dH(h)}{dh}, \end{aligned} \tag{1}$$

where $P'(h)$ represents total strain gradient, $S'(h)$ represents elastic total strain gradient, $E'(h)$ represents elastic normal strain gradient, and $H'(h)$ represents plastic total strain gradient induced beneath the indenter; h is the penetration depth. We will further refer to these functions as the corresponding strain gradients instead of strain gradient representations because they differ by a constant factor only. The specialized total, $P''(h)$, elastic total, $S''(h)$, elastic normal, $E''(h)$, and plastic total, $H''(h)$ divergences are given by

$$\begin{aligned} P''(h) &\equiv \nabla P'(h), \\ S''(h) &\equiv \nabla S'(h), \\ E''(h) &\equiv \nabla E'(h), \\ H''(h) &\equiv \nabla H'(h). \end{aligned} \tag{2}$$

For further details on the derivation and discussion of Eqs. 1–2 and on the practical calculation of the stress-strain field gradient and divergence representations cf. Ref. 7.

3. RESULTS AND DISCUSSION

SSF gradient and divergence oscillations induced by nanoindentation were observed in all the examined steel, silicon, glass and silica samples and they manifested similar strain hardening-softening cycles when the sharp Berkovich indenter penetrated the subsurface layer. Results on the bulk solid sample of silicon were reported in the first part of this investigation [7]. For the clarity of the discussion we focus here on reporting a few typical results of the nanoindentation measurements of the CZS sample, which are representative of all the steel samples examined in our investigation. In addition, results from the well-known and widely used reference material fused silica are also displayed to showcase the generality of the SSF gradient-divergence oscillation phenomenon. We also provide a preliminary quantitative analysis of the oscillations.

3.1 SSF Gradient and Divergence Oscillations

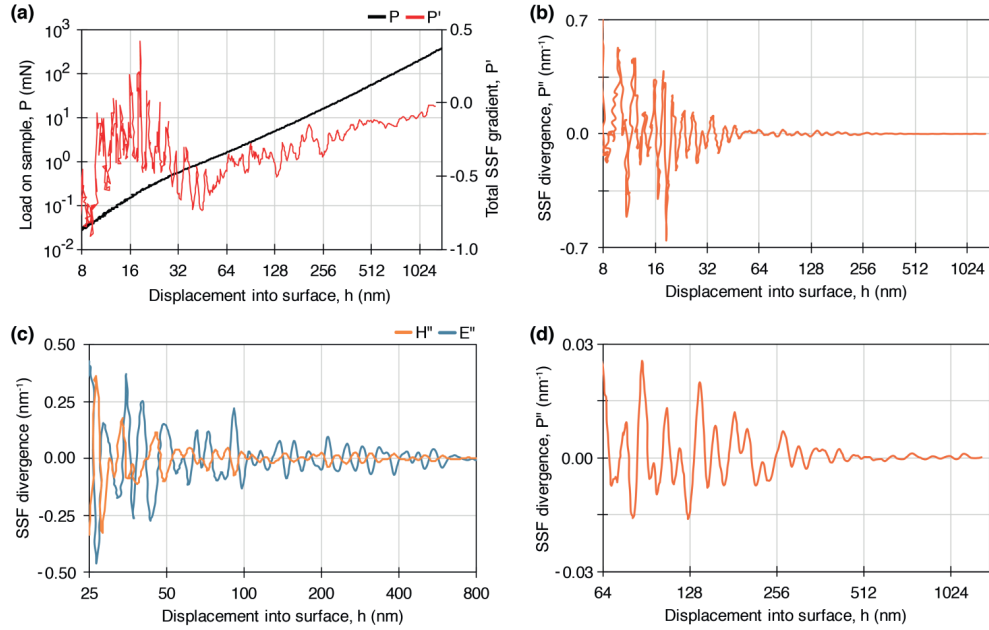


Fig. 1. Total stress-strain field gradient and divergence oscillations in the CZS sample:
(a) A typical example of the load-displacement, P - h , curve (black) and the total SSF gradient, P' - h , curve (gray) obtained from a single indentation test in the CSM mode;
(b) Total SSF divergence oscillations obtained from the same measurement;
(c) Plastic normal (H'' - h curve, gray) and elastic normal (E'' - h curve, black) SSF divergence oscillations calculated from the same measurement;
(d) Close-up of the total SSF divergence low amplitude oscillations from (b) at larger penetration depths.

Figure 1(a) shows a typical example of a single nanoindentation test measurement (as opposed to an averaged measurement) in the CSM mode of the CZS steel sample. The load-displacement curve is contrasted with the corresponding total SSF gradient curve, which was derived using the approach briefly outlined in Methods (see also Ref. 7). Note that we use logarithmic axis for the displacement into surface, h , to highlight nanoindentation responses at the subsurface layers. Clear oscillations of the SSF gradient can be observed already starting from 8 nm depth despite the measurement noise. The total SSF divergence oscillations are shown in Fig. 1(b). Very similar oscillations were observed for all 19 single nanoindentation tests of the CZS steel sample. The SSF gradient-divergence oscillations were observed throughout the indentation measurement, even at large indenter penetration depths (see Fig. 1(d), where the SSF divergence oscillations are present at up to more than 1000 nm). Therefore, they cannot be solely attributed to the structural inhomogeneities related to surface roughness, which based on the RMS measurements was only 2–3 nm, or the superficial layer.

The oscillations of the strain gradient might be caused by alternating normal-shear strain transformation processes converting strains into each other: as the sharp Berkovich indenter penetrates the sample the normal strain builds up until the sample structure cannot withstand it anymore and some sliding of elastically deformed region occurs, i.e., shear strain leads to plastic deformation. Furthermore, the incremental stresses induced by indenter interact with the structural stresses inherent in the subsurface layer. The amplitude of the SSF gradient-divergence oscillations is larger closer to the surface, where free- and near-surface layer acts as a large structural defect in comparison with the atomic structure in bulk. Subsequently, the amplitude decayed rather rapidly as the indenter penetrated deeper into the sample and approached its bulk structure that was far enough from the free surface.

Figure 1(c) shows the total plastic SSF divergence, H'' - h curve, and the elastic normal SSF divergence, E'' - h curve, that were derived from the hardness and elastic modulus indentation datasets, respectively. Divergences $H''(h)$ and $E''(h)$ tells us at which h values the interface between the hydrostatic core and the plastic deformation zone acts as a stress-strain flux source or sink. Therefore, depth intervals where the divergence of the corresponding component of the SSF is positive can be interpreted as strain hardening of the sample subsurface layer. Within these depth intervals, the subsurface layer acts as a SSF flux source. Similarly, the penetration depth intervals of negative divergence can be interpreted as strain softening of the subsurface layer. In turn, the plastic deformation zone underneath the indenter acts as a stress-strain flux sink. The oscillations in Fig. 1(c) reveal a structure of strain hardening-softening zones induced by the sharp Berkovich indenter. The oscillations of the elastic and plastic SSF divergences were out of phase, which indicated that elastic and plastic deformation processes in the subsurface layer happened in an alternating fashion. This is in a good agreement with the physical nature of the elastic-plastic deformation where plastic deformation processes follow the elastic ones regardless of the specific mechanism. The sample in the subsurface layer is expected to be rather heterogeneous having different sized nanograins, nanoparticles, dislocations within nanocrystallites, nanovoids, etc. This gives rise to many different specific plastic deformation mechanisms that might occur underneath the loaded indenter during the nanoindentation experiment: slipping, twinning, cold working, grain boundary

sliding, strain bursts or flow serrations, shear band formation, stick and slip events, among others [8]–[10], [13], [14]. For example, nanovoids can be frequently present, which then can be packed by the applied load during the indentation process. The process of packing is largely a plastic deformation causing a strain hardening effect, which is indicated by the positive divergence of the plastic SSF divergence ($H''(h) > 0$). However, any discrete plastic deformation event has its own early elastic phase manifested here by the overtaking positive elastic SSF divergence ($E''(h) > 0$). Elastic phase can happen only up to the point where the elastic limit has not exceeded yet. After the local yield point is reached, the elastic strain triggers the corresponding plastic one. Yielding and hardening effects lead to further development of plastic strain under load. However, progressing plastic strain thereafter discharges the preceding elastic stresses as it is shown by the out-of-phase oscillations of $E''-h$ and $H''-h$ curves in Fig. 1(c). In turn, strain-softening effect may occur after grain boundary sliding when some portion of the substance is pushed out of the plastic zone underneath the indenter and internal elastic pressure thereafter drops down. Of course, the grain boundary sliding event has its own early elastic phase as well.

3.2 SSF Gradient and Divergence from Averaged Datasets

The SSF gradient calculated from the averaged load-displacement curves of the CZS sample was much smoother than in the single measurements and the oscillations were practically not visible (Fig. 2). SSF divergence oscillations could still be detected albeit they were markedly smaller in amplitude compared to the single tests (Fig. 3). The strain hardening-softening zones (HSZ) in Fig. 3 are highlighted by applying the sign function on the corresponding components of SSF divergence (e.g., $HSZ(E'') = \text{sign}(E'')$), revealing similar pattern seen in the case of single measurements: the strain hardening ($HSZ > 0$) and softening ($HSZ < 0$) cycles of the elastic and plastic components of SSF divergence tend to happen in an alternating fashion. However, generally the attempts to detect strain gradient-divergence oscillations from the averaged dataset will be impaired because the oscillations of the single indentation tests are shifted in phase with respect to each other and averaging will to a large extent smoothen them out. However, less subtle fluctuations, e.g., due to a layered atomic microstructure in the case of thin films may still be detectable with the strain gradient-divergence approach also in the averaged indentation dataset [15]. For example, the averaged SSF gradient curve for the CZS steel had a pronounced convex shape (see Fig. 2), which is in a good agreement with the model where the subsurface layer plays role of the skin of bulk materials and it has to endure a very large pressure difference between the outside and inside of the bulk sample (i.e., the skin effect). This is easy to understand as the pressure at the free surface of the sample is about 0.1 MPa, whereas the pressure inside the bulk samples reaches values of about 1000 MPa and higher. The pressure between the outside and inside of the sample differs on the order of 10^4 – 10^5 times, which makes the atomic layers within the subsurface area very stressed in comparison with those lying deeper inside the sample, far away from the free surface. The stresses within the subsurface layer are lowering when indenter is loading the surface of the bulk sample, which can be interpreted as strain softening of the subsurface layer at the beginning phase of the nanoindentation measurement.

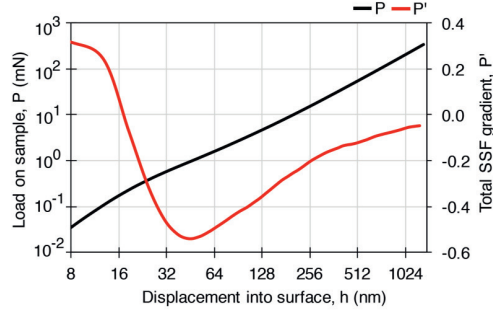


Fig. 2. The strain gradient oscillations of the CZS steel sample are smoothed out when the total strain gradient-displacement, $P'-h$, curve (gray) is calculated from the averaged ($n=19$) load-displacement, $P-h$ (black).

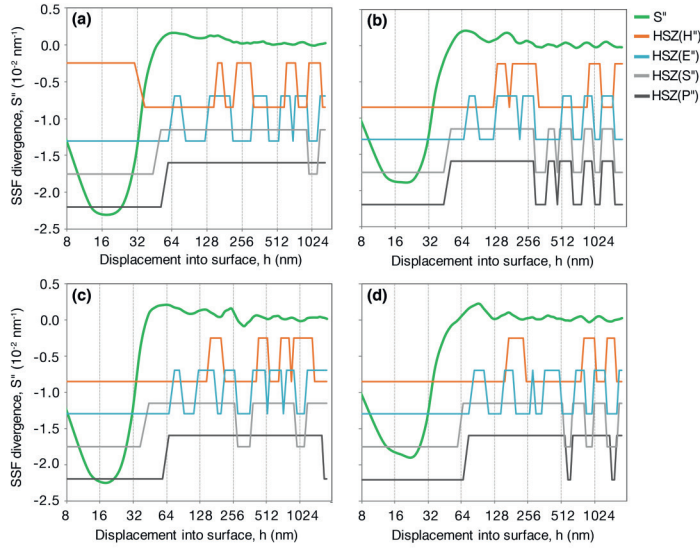


Fig. 3. SSF divergence oscillations are also present, albeit much less prominently, in the averaged nanoindentation datasets of the steel samples: (a) CZS, (b) 100Cr6, (c) SCH, (d) HGV. Total elastic SSF divergence, $S''-h$, curve is shown together with the strain hardening-softening zones (HSZ) of the corresponding SSF divergence components; the HSZ curves are vertically offset for presentation purposes.

3.3 Additional Tests for the Presence of Strain Gradient Oscillations

In the CSM mode, weak superimposed oscillations are applied additionally to the load-time frame in order to measure the apparent hardness and elastic modulus throughout the loading process. This might in principle introduce some fluctuations of the sample mechanical properties and potentially even alter the indentation measurement results [16]. The CSM mode oscillations happen on a much faster time-scale than the strain gradient-divergence oscillations and thus it was highly unlikely that CMS mode could affect the results. However, to confirm that the stress-strain gradient oscillations are not an artefact of the CSM loading mode, additional nanoindentation tests were made in the so-called BASIC mode, where the applied load was increasing up to the maximum load without any superimposed shallow oscillations

during the loading process. Figure 4(a) shows that the stress-strain field gradient exhibits clear oscillations also when the indentation experiment is carried out in the BASIC mode.

Subsurface layer mechanics of steel samples may differ from that of glass samples because the surface of steel samples needs grinding and polishing before it is possible to carry out nanoindentation experiments. In turn, grinding and polishing of the steel sample may result in, e.g., Beilby layer having somewhat specific structure and mechanics [17], [18]. In contrast, glass samples in most cases do not need a special treatment of the surface after they are manufactured from the glass liquid phase. To test whether the SSF gradient oscillations are not just a peculiarity of the steel material, we indented a sample of a well-known reference material, the fused silica. Prominent stress-strain field gradient oscillations were present in all eight single indentation tests we performed (see Fig. 6(b) for a typical example).

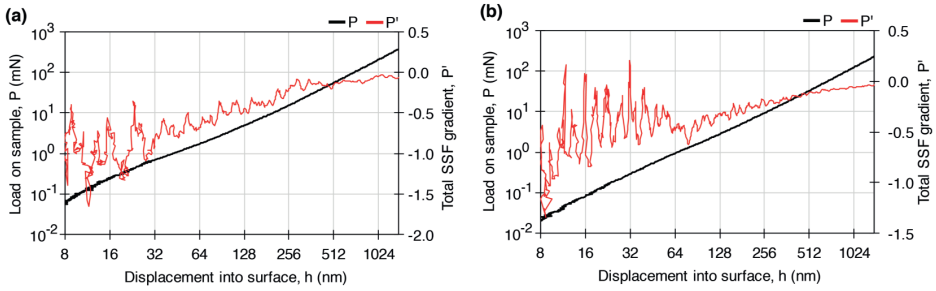


Fig. 4. Additional tests of the strain gradient oscillation phenomenon: the load-displacement, P - h , curve (black) and the total SSF gradient, P' - h , curve (gray) from a typical single measurement in (a) CZS steel in BASIC mode and (b) fused silica in CSM mode.

3.4 Quantitative Features of the Oscillations

Are the stress-strain field gradient-divergence oscillations specific for each material? We compared the decay behavior of the total plastic SSF divergence oscillations of CZS steel and fused silica by finding the positive peaks of H'' - h curves, $H''_{peak}(h)$, and plotting them against the penetration depth, h (Fig. 5). $H''_{peak}(h)$ was defined as the maximum positive value between two consecutive crossings of the displacement h -axis of the H'' - h curve. The amplitude of oscillations for the steel sample was generally lower except at very shallow penetration depths. The amplitude for both materials decayed monotonically with increasing penetration depth. However, there appear to be two different stages of oscillations: an initial stage of gradually decaying, higher amplitude oscillations followed by a rather sharp, discontinuous drop in amplitude at a penetration depth of approximately $h=30$ nm for the CZS sample and $h=60$ nm for the fused silica. After the sharp decrease, the amplitude again continues to decay more gradually. The smaller amplitude oscillations appear to decay to the first approximation as a power-law, i.e., $H''_{peak}(h) \propto h^\alpha$, with the exponent $\alpha = -0.9$ and $\alpha = -0.8$ for steel and fused silica, respectively. Interestingly, the half-wave length of the $H''(h)$ oscillations, $\lambda_{1/2}(h)$, defined as the distance in h between two consecutive crossings of the h -axis, increased linearly with increasing penetration depth for both steel and fused silica (Fig. 6). Alternatively, the half-wave

length can be expressed as a function of the wave number, N , in which case $\lambda_{1/2}(N)$ grows exponentially.

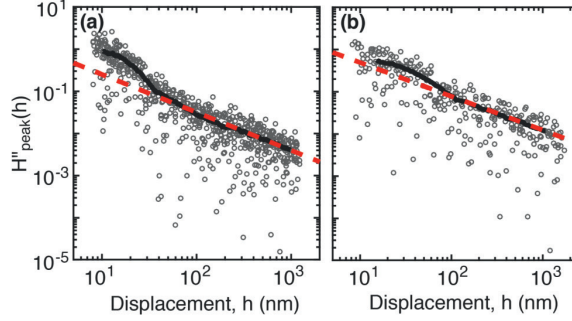


Fig. 5. $H''(h)$ peak amplitude, $H''_{peak}(h)$, as function of the penetration depth, h , for (a) steel ($n=19$ tests) and (b) fused silica ($n=8$ tests). Gray open circles are pooled data from all tests; black, solid lines show a moving average over 60 points of the pooled and sorted dataset to reveal the trend of the $H''_{peak}(h)$ decay; gray, dashed line demonstrates a power-law relationship $H''_{peak}(h) \propto h^\alpha$ with the exponent $\alpha = -0.9$ in (a) and $\alpha = -0.8$ in (b).

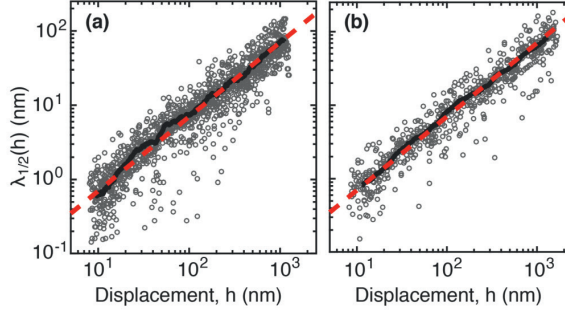


Fig. 6. Half-wave length of the $H''(h)$ oscillations, $\lambda_{1/2}(h)$, as a function of the penetration depth, h , for (a) steel ($n=19$ tests) and (b) fused silica ($n=8$ tests). Gray open circles are pooled data from all tests; black, solid line shows a moving average over 60 points of the pooled and sorted dataset to reveal the trend of the $\lambda_{1/2}(h)$ growth; gray, dashed line demonstrates a linear relationship $\lambda_{1/2}(h) \propto h$ in both (a) and (b).

Overall, the analysis suggests that the SSF divergence oscillations have a quasi-regular, material specific structure with the amplitude and period changing in a regular manner, which follows a well-defined mathematical relationship with respect to the indentation depth. However, further investigations together with more detailed morphological assessment techniques as a reference (e.g., using cross-sectional transmission electron microscopy [19]) are necessary to elucidate oscillation features pertaining to specific mechanical properties of the sample subsurface layer.

4. CONCLUSIONS

We have found that nanoindentation experiment with a sharp Berkovich indenter induces SSF gradient-divergence oscillations in the bulk solids. The oscillations are especially prominent at low indentation depths (< 100 nm) indicating that they are primarily a property of the bulk solid subsurface layer. The oscillation

amplitude decays rapidly as the indenter approaches deeper atomic layers, but some fluctuations can still be detected even at displacements greater than 1000 nm. We have interpreted the oscillations as alternating strain hardening and softening cycles taking place in the subsurface layers under the indenter load. The fading of the oscillations at deeper atomic layers of the sample (i.e., closer to the “in bulk” region) manifests that deformation processes underneath the indenter have reached a steady state where the nanohardness and elastic modulus do not change anymore under continued loading of the sample. Although the elastic and plastic stress-strain fields are superimposed, it was possible to separate their respective components and study elastic and plastic deformation processes selectively. We have observed that elastic and plastic strain hardening and softening cycles happen in an alternating fashion, which agrees with the nature of elastic-plastic deformation.

The strain hardening-softening oscillations have been observed in all the studied samples. Steel has a polycrystalline lattice structure, whereas glass is an amorphous material, and the specific deformation mechanisms in both types of materials can be different. However, these results suggest that the alternating cycles of work hardening and softening effects are a general phenomenon occurring in bulk solids when their surface is loaded by the incremental stress. Preliminary quantitative analysis suggests that the oscillations have features that are typical of different materials, but further investigations, preferably together with detailed morphological characterization of the sample microstructure are necessary to fully discover the potentially valuable information about the mechanical properties of the material subsurface layer hidden in the strain gradient-divergence oscillations.

ACKNOWLEDGEMENTS

The authors thank Dr. Roberts Zabels at the Institute of Solid State Physics, University of Latvia for providing the datasets of the nanoindentation and AFM experiments, and Prof. Janis Maniks for encouraging and helpful discussions.

REFERENCES

1. Fischer-Cripps, A. (2004). *Nanoindentation*. New York: Springer-Verlag.
2. Oyen, M.L., & Cook, R.F. (2009). A practical guide for analysis of nanoindentation data. *J. Mech. Behav. Biomed.*, 2, 396–407.
3. Guo, Y.B., & Warren, A.W. (2005). Microscale mechanical behavior of the subsurface by finishing processes. *J. Manuf. Sci. Eng.*, 126, 333–338.
4. Warren, A.W., Guo, Y.B., & Weaver, M.L. (2006). The influence of machining induced residual stress and phase transformation on the measurement of subsurface mechanical behavior using nanoindentation. *Surf. Coat. Tech.*, 200, 3459–3467.
5. Michel, J.P., Ivanovska, I.L., Gibbons, M.M., Klug, W.S., Knobler, C.M., Wuite, G.J.L., & Schmid, C.F. (2006). Nanoindentation studies of full and empty viral capsids and the effects of capsid protein mutations on elasticity and strength. *Proc. Natl. Acad. Sci. USA*, 103, 6184–6189.
6. Sangwal, K. (2000). On the reverse indentation size effect and microhardness measurement of solids. *Mater. Chem. Phys.*, 63, 145–152.

7. Kanders, U., & Kanders, K. (2017). Nanoindentation response analysis of thin film substrates-I: Strain gradient-divergence approach. *Latv.J. Phys.Tech. Sci.*, 54(1), 66–76, DOI: 10.15.15/lpts-2017-0007
8. Klaumuenzer, D., Maass, R., & Loeffler, J.F. (2011). Stick-slip dynamics and recent insights into shear banding. *J. Mater. Res.*, 26, 1453–1463.
9. Schuh, C.A., & Nieh, T.G. (2003). A nanoindentation study of serrated flow in bulk metallic glasses. *Acta Mater.*, 51, 87–99.
10. Chakraborty, R., Dey, A., & Mukhopadhyay, A.K. (2010). Loading rate effect on nano-hardness of soda-lime-silica glass. *Metall. Mater. Trans. A* 41, 1301–1312.
11. Hay, J.L., Agee, P., & Herbert, E.G. (2010). Continuous stiffness measurement during instrumented indentation testing. *Exp. Techniques*, 34, 86–94.
12. Oliver, W., & Pharr, G. (2004). Measurement of hardness and elastic modulus by instrumented indentation: advances in understanding and refinements to methodology. *J. Mater. Res.*, 19, 3–20.
13. Li, H., Ngan, A.H.W., & Wang, M.G. (2005). Continuous strain bursts in crystalline and amorphous metals during plastic deformation by nanoindentation. *J. Mater. Res.*, 20, 3072–3081.
14. Maniks, J., Mitin, V., Kanders, U., Kovalenko, V., Nazarovs, P., Baitimirova, M., Meija, R., Zabels, R., Kundzins, K., & Erts, D. (2015). Deformation behavior and interfacial sliding in carbon/copper nanocomposite films deposited by high power DC magnetron sputtering. *Surf. Coat. Tech.*, 276, 279–285.
15. Kanders, U., Kanders, K., Maniks, J., Mitin, V., Kovalenko, V., Nazarovs, P., & Erts, D. (2015). Nanoindentation response analysis of Cu-rich carbon–copper composite films deposited by PVD technique. *Surf. Coat. Tech.*, 280, 308–316.
16. Siu, K.W., & Ngan, A.H.W. The continuous stiffness measurement technique in nanoindentation intrinsically modifies the strength of the sample. *Philos. Mag.*, 93, 449–467.
17. Beilby, G. (1921). *Aggregation and Flow of Solids*. London: Macmillan.
18. Bhushan, B. (Ed.) (2001). *Modern Tribology Handbook*. CRC Press.
19. Lloyd, S.J., Castellero, A., Giuliani, F., Long, Y., McLaughlin, K.K., Molina-Aldareguia, J.M., Stelmashenko, N.A., Vandeperre, L.J., & Clegg, W.J. (2005). Observations of nanoindentations via cross-sectional transmission electron microscopy: A survey of deformation mechanisms. *Proc. R. Soc. A*, 461, 2521–2543.
20. Misra, A., Verdier, M., Lu, Y.C., Kung, H., Mitchell, T.E., Nastasi, M., & Embury, J.D. (1998). Structure and mechanical properties of Cu-X (X= Nb, Cr, Ni) nanolayered composites. *Scripta Mater.*, 39, 555–560.

VAKUUMA PĀRKLĀJUMU SUBSTRĀTU NANOIDENTĒŠANAS DATU ANALĪZE-II: UZKALDINĀŠANAS-ATKALDINĀŠANAS OSCILĀCIJAS PIEVIRSMAS SLĀNĪ

K o p s a v i l k u m s

Šajā pētījumā analizēti dažādu tēraudu, stikla un kausēta kvarca masīvu paraugu pievirsma deformācijas procesi. Tā kā minētie materiāli parasti tiek izmantoti kā substrāti plānu vakuuma pārklājumu izgulsnēšanai, tad pētījuma rezultāti ir aktuāli arī plāno kārtiņu fizikas un mikroelektronikas nozarēs. No nanoindentēšanas eksperimenta datiem tika izskaitļots indentēšanas radītais deformācijas gradients un

divergence. Deformācijas gradienta un diverģences oscilācijas norādīja uz dinamiskiem procesiem, kas saistīti ar materiālu lokāliem uzkaldināšanas un atkaldināšanas procesiem pievirsmas slānī. Uzkaldināšanas-atkaldināšanas procesu dinamika sevišķi spilgti bija izteikta pie maziem iespiešanās dziļumiem ($h < 100$ nm). Augot h , to amplitūda pakāpeniski samazinājās, taču tika novērota pat līdz $h = 1000$ nm un vēl lielākiem indentora iespiešanās dziļumiem.

22.02.2017.

RESEARCH OF SURFACE ROUGHNESS ANISOTROPY

N.Bulaha, J.Rudzitis, J.Lungevics, O.Linins, J.Krizbergs

Institute of Mechanical Engineering,

Riga Technical University,

6 Ezermalas Str., LV-1006, Riga, LATVIA

e-mail: mti@rtu.lv

The authors of the paper have investigated surfaces with irregular roughness for the purpose of determination of roughness spacing parameters perpendicularly to machining traces – RSm_1 and parallel to them – RSm_2 , as well as checking the relationship between the surface anisotropy coefficient c and surface aspect ratio Str from the standard LVS EN ISO 25178-2. Surface roughness measurement experiments with 11 surfaces show that measuring equipment values of mean spacing of profile irregularities in the longitudinal direction are not reliable due to the divergence of surface mean plane and roughness profile mean line. After the additional calculations it was stated that parameter Str can be used for determination of parameter RSm_2 and roughness anisotropy evaluation for grinded, polished, friction surfaces and other surfaces with similar characteristics.

Keywords: *anisotropy coefficient, roughness spacing parameters, surface texture, texture aspect ratio.*

1. INTRODUCTION

Analysis of surface roughness spacing parameters [1] provides that for surfaces with irregular roughness spacing parameters values occasionally are not reliable due to the fact that mean plane of surface roughness and the roughness profile mean line are located at different levels, in particular, it is expressed for mean spacing of profile irregularities in the longitudinal direction. Thereby difficulties with surface anisotropy evaluation are arising.

In order to solve the existing problems, scientists offer using the visual method, which will allow identifying more reliable values of spacing parameters RSm_1 and RSm_2 . In addition, it is reasoned that the surface roughness anisotropy can be described by the surface aspect ratio Str from standard EN ISO 25178-2: 2012 [2], which is essentially equal to the roughness anisotropy coefficient c .

$$Str = c. \quad (1)$$

By contrast, variants of surface roughness anisotropy evaluation offered in [1]

are justified only in theory, which is why it is important to prove them with practical experiments.

2. EXPERIMENTAL PART

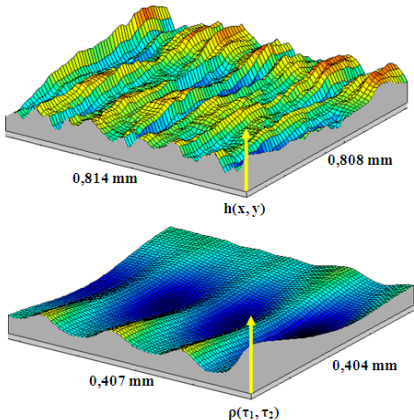
To test relation (1) according to which, with specially oriented surface roughness correlation function $\rho(\tau_1, \tau_2)$ [3], texture aspect ratio Str is equal to surface roughness anisotropy coefficient c , the authors of the paper have studied 11 surfaces obtained by different technological methods (see Table 1 and Table 2).

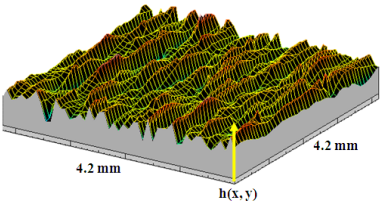
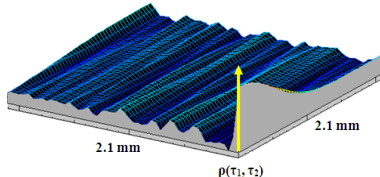
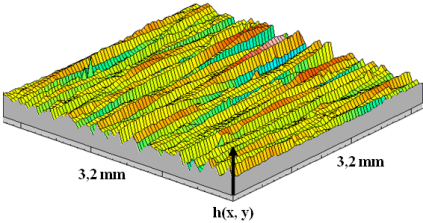
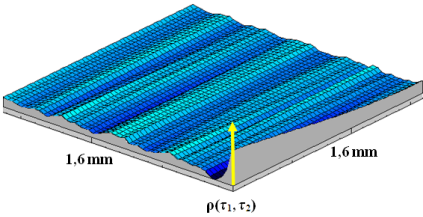
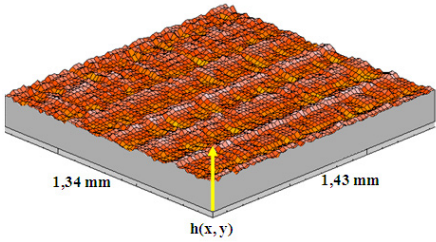
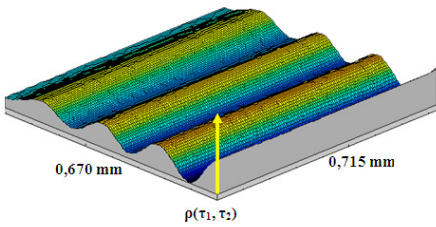
Surface roughness measurement experiment was carried out on the profilograph-profilometer Taylor Hobson Talysurf Intra 50. It is the measuring equipment that provides determination of surface roughness parameters in the 3-D coordinate system. Before the start of the experiment, the 2-D surface roughness measurements were made in order to determine the sample and evaluation length for each sample surface. In addition, a required number of points – 300 points – were chosen, considering the developed methodology mentioned in [4]. After the roughness measurement experiment, the filtering of obtained surface topography was carried out to make surface leveling and separate from it form and waviness occurring at various mechanical machining conditions (part clamping, deflection, thermal processes, vibrations and the cutting-tool path deviation). After surface filtration, the 3D roughness parameters and additional profile parameters, which were extracted from different surface cross sections, were determined. The values provided in Table 1 and Table 2 are mean values obtained from three measurements of surfaces.

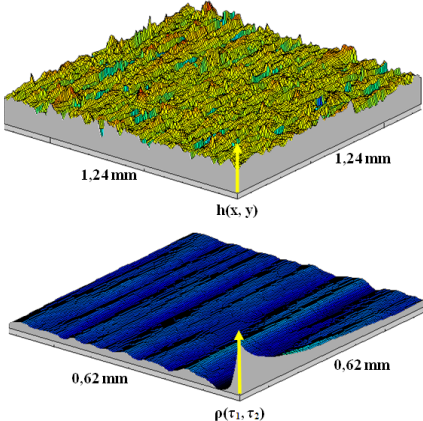
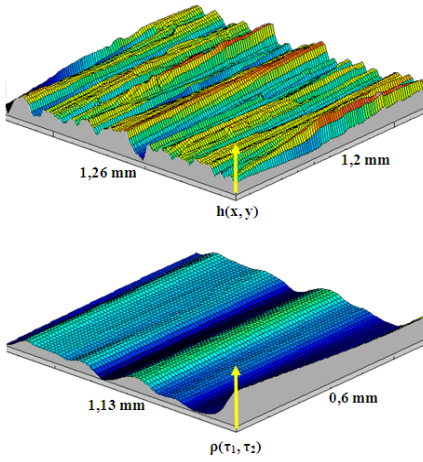
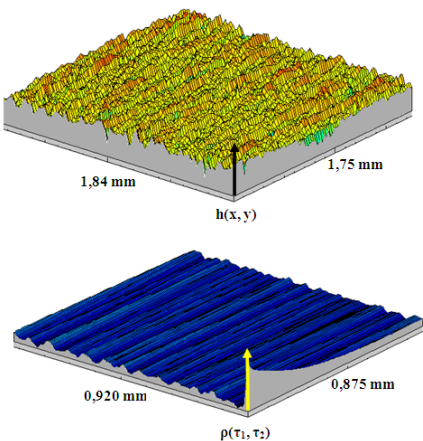
Table 1 contains images of each 3D surface roughness $h(x, y)$ and 3D surface roughness autocorrelation function $\rho(\tau_1, \tau_2)$ in order to show the characteristics of the technological process. Parameter Sa is provided as well, but in crosswise direction 1 (crosswise to machining (friction) traces) and in longitudinal direction 2 – parameters Ra_1 , Ra_2 .

Table 1

Comparison between 3D and 2D Height Parameters of Irregular Surface Roughness

Machining	Topography, correlation function	$Sa, \mu m$	$Ra_1, \mu m$	$Ra_2, \mu m$
1. Surface grinding (Rugotest No. 104, surface No.3)		0.048	0.036	0.008

Machining	Topography, correlation function	$Sa, \mu\text{m}$	$Ra_1, \mu\text{m}$	$Ra_2, \mu\text{m}$
2. Surface grinding (Rugotest No.104, surface No.7)	 	1.410	1.115	0.140
3. Surface grinding (Rugotest No.104, surface No.8)	 	3.130	2.660	0.229
4. Cylindrical grinding (Rugotest No.105, surface No.1)	 	0.028	0.018	0.015

Machining	Topography, correlation function	$Sa, \mu\text{m}$	$Ra_1, \mu\text{m}$	$Ra_2, \mu\text{m}$
5. Cylindrical grinding (Rugotest No.105, surface No.4)		0.174	0.143	0.058
6. Cylindrical grinding (Rugotest No.105, surface No.8)		3.500	3.487	0.715
7. Surface after the sliding experiment		0.077	0.071	0.025

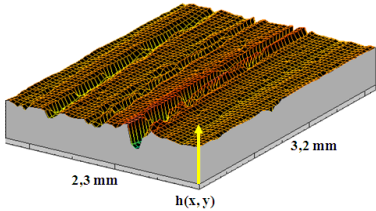
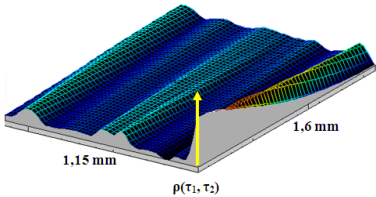
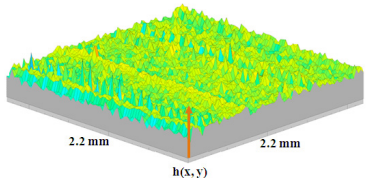
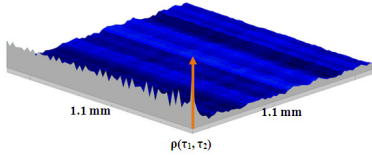
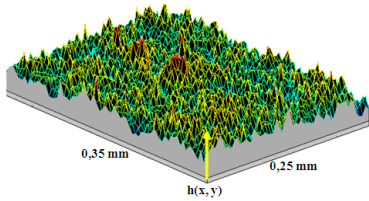
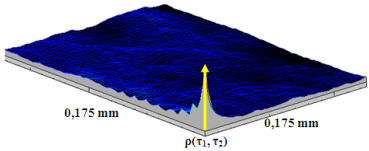
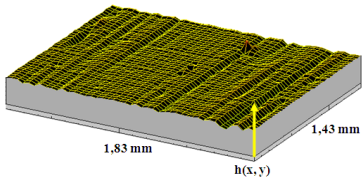
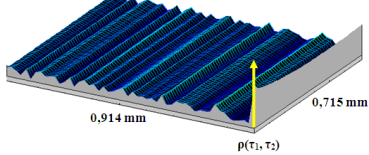
Machining	Topography, correlation function	$Sa, \mu\text{m}$	$Ra_1, \mu\text{m}$	$Ra_2, \mu\text{m}$
8. Surface after finishing the sliding friction	 	0.674	0.517	0.061
9. Lapping	 	0.133	0.102	0.081
10. Nano-coating	 	0.612	0.082	0.085
11. Polishing (bobsled runner)	 	0.127	0.107	0.022

Table 2 comprises mean spacing of profile elements RSm_1 and RSm_2 , and surface anisotropy characteristics Str and c . Furthermore, mean spacing of profile irregularities RSm_2 was acquired using 2 methods: using measuring equipment Taylor Hobson Intra 50 (RSm_2 – mean spacing of profile irregularities in longitudinal direction measured with the measuring equipment) and using visual determination method ($[RSm_2]_{viz}$ – mean spacing of profile irregularities in longitudinal direction determined by visual inspection). It should be noted that based on evaluation given by 5 specialists the visual method allows one to determine RSm values with a 10 % margin of error. The error is not small; however, it produces better results than using an incorrect value of mean spacing of profile irregularities.

Table 2

Analysis of irregular surface roughness spacing parameters

No.	Machining	RSm_1 , mm	RSm_2 , mm	$[RSm_2]_{viz}$, mm	Str	c
1.	Surface grinding (Rugotest 104, surface No.3)	0.088	0.131	0.400	0.144	0.150
2.	Surface grinding (Rugotest 104, surface No.7)	0.140	0.348	4.200	0.031	0.033
3.	Surface grinding (Rugotest No.104, surface No.8)	0.095	0.087	3.200	0.024	0.029
4.	Cylindrical grinding (Rugotest No.105, surface No.1)	0.073	0.051	1.430	0.055	0.051
5.	Cylindrical grinding (Rugotest No.105, surface No.4)	0.059	0.101	1.250	0.047	0.047
6.	Cylindrical grinding (Rugotest No.105, surface No.8)	0.080	0.141	1.200	0.063	0.066
7.	Surface after the sliding experiment	0.029	0.031	1.750	0.013	0.016
8.	Finishing	0.100	0.160	3.200	0.029	0.031
9.	Lapping	0.049	0.044	0.157	0.333	0.312
10.	Nano-coating	0.016*	0.011	0.025	0.612	0.640
11.	Polishing (bobsled runner)	0.030	0.032	1.430	0.018	0.021

*Determined by visual inspection

In Table 1, values of profile parameters Ra_1 and Ra_2 were compared with Sa values for each machining type. If these parameters are close in their numerical value (more precisely – have the same order of magnitude), it means that the mean lines of the corresponding profiles are positioned close to the mean plane of roughness, spacing parameters of these profiles can be considered probable for the mean plane level and, therefore, they characterise 3D roughness surface. If that is not the case, RSm_1 and RSm_2 values are determined visually.

In crosswise direction, there is only one surface (nano-coated) with values of parameter Ra_1 significantly different from value of parameter Sa . In this case,

parameter RSm_1 cannot be considered as belonging to the level of the mean plane and cannot be used for calculation of anisotropy coefficient c . RSm_1 value of this surface was determined visually.

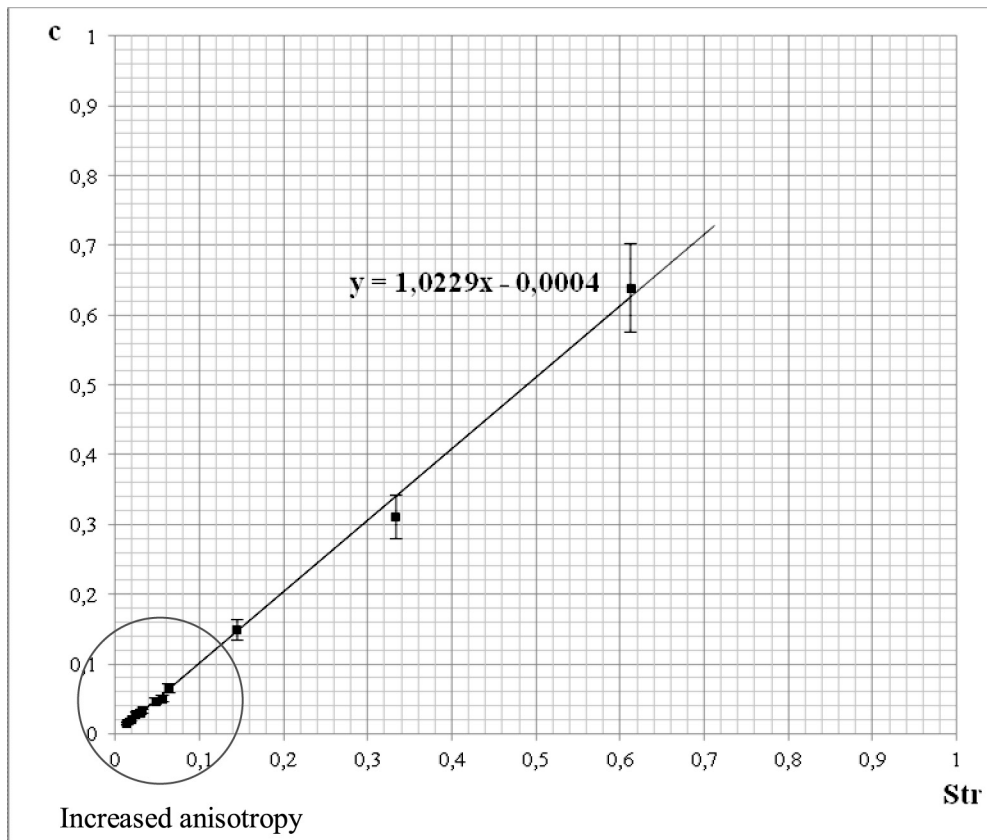
As for the other surfaces, RSm_1 values obtained with the measuring equipment were eligible for usage in calculating c according to formula (1).

Parameter RSm_2 used in formula (1) is determined in a similar manner. If $Ra_2 \approx Sa$, parameter RSm_2 obtained with the measuring equipment can be used to calculate anisotropy coefficient c , if $Ra_2 \ll Sa$, this means spacing of profile irregularities is determined visually and is written as $[RSm_2]_{viz}$. As shown in Table 2, all 11 surfaces required $[RSm_2]_{viz}$ value to be determined.

When the values of mean spacing of profile elements are obtained, anisotropy coefficient c is calculated according to formula [1]:

$$c = \frac{RSm_1}{RSm_2}. \quad (2)$$

The calculated c values are compared to values of 3D surface texture aspect ratio Str (see Fig. 1).



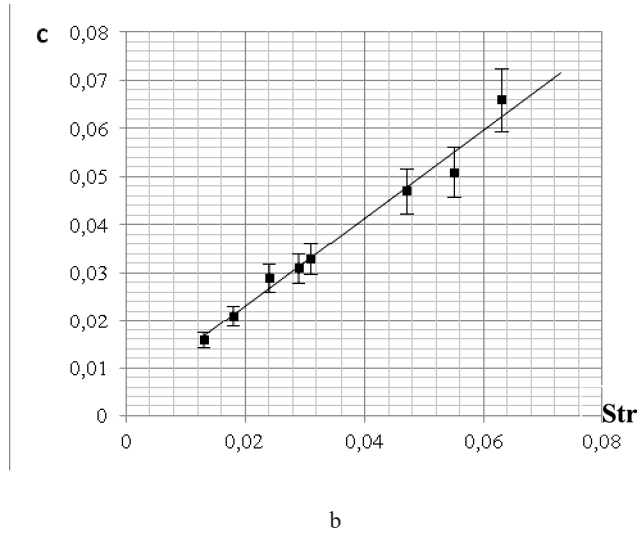


Fig. 1. Relationship between parameters c and Str (with \pm marked visual detection error range of parameter c): a – the whole surface, b – surfaces with increased anisotropy.

Data provided in Fig.1 reflect formula (1) reasonably accurately. It is clearly seen in surfaces with anisotropy coefficient $c < 0.1$ (surfaces with increased anisotropy). Autocorrelation function of these surfaces is notably oriented along crosswise and longitudinal profiles.

3. EVALUATION METHODOLOGY FOR ANISOTROPY

Surface roughness anisotropy can be evaluated following the steps listed below:

1. Create 3D surface roughness topography.
2. Determine surface texture parameters Sa and Str .
3. Chose surface sections that are perpendicular and parallel to the traces of surface machining.
4. Determine height parameters Ra_1 and Ra_2 for surface roughness profiles and spacing parameters RSm_1 and RSm_2 .
5. Compare mean values of Ra_1 and Ra_2 of the profiles with surface texture parameter Sa .
 - 5.1. If values of both parameters are close to or almost the same as Sa values, it can be considered that the mean lines of all profiles are located at the mean plane level and, thus, it can be assumed that RSm_1 and RSm_2 values characterise the surface.
 - 5.2. If parameter Ra_1 is close to Sa in value while parameter Ra_2 significantly differs, mean spacing of profile elements RSm_2 is determined using surface texture aspect ratio by formula: $RSm_2 = RSm_1 / Str$.
 - 5.3. If neither of the parameters (Ra_1 and Ra_2) is close to Sa value, anisotropy is evaluated using the visual method and formula (1): $c = RSm_1 / Rsm_2$.

4. CONCLUSIONS

Within the present research, the analysis of roughness anisotropy for 11 surfaces with irregular character has been made. Firstly, anisotropy coefficient c has been calculated by measuring mean spacing of profile irregularities for surface roughness using measuring equipment Taylor Hobson Talysurf Intra 50 and, in addition, using the visual method, when a mean line of a profile and mean plane of a surface are at different levels. Then the calculated values of anisotropy coefficient c have been compared to the values of surface texture aspect ratio Str . During the research, it has been established that surface texture parameter Str can be applied to surface roughness anisotropy analysis and calculations of mean spacing of profile irregularities. In the research, the methodology for surface roughness anisotropy determination has been proposed.

REFERENCES

1. Rudzitis, J., Bulaha, N., Lungevics, J., Linins, O., & Berzins, K. (2017). Theoretical analysis of spacing parameters of anisotropic 3D surface roughness. *Latvian Journal of Physics and Technical Sciences*, 54(2), pp., 55-63.
2. International Organization for Standardization. (2012). Geometrical product specifications (GPS) – Surface texture: Areal – Part 2: Terms, definitions and surface texture parameters. ISO 25178-2:2012.
3. Rudzitis, J. (2007). *Mechanics of Surface Contact. Part 1. Parameters of Surface Roughness Profile*. Riga: Riga Technical University (in Russian).
4. Bulaha, N., Rudzitis, J., Lungevics, J., & Cudinovs, V. (2016). Measurement principles of 3D roughness parameters. In *15th International Conference "Engineering for Rural Development"*, 25–27 May 2016 (pp.1059–1064). Latvia, Jelgava: Latvia University of Agriculture, Latvia.

VIRSMAS RAUPJUMA ANIZOTROPIJAS IZPĒTE

J.Rudzitis, N.Bulaha, J.Lungevičs, O.Liniņš, J. Krizbergs

Kopsavilkums

Dotajā rakstā tika veikti virsmu ar neregulāru raupjumu pētījumi, ar mērķi noteikt raupjuma soļa parametrus perpendikulāri apstrādes pēdām RSm_1 un paralēli tām – RSm_2 , kā arī pārbaudīt sakarību starp virsmas anizotropijas koeficientu c un virsmas tekstūras indeksu Str no LVS EN ISO 25178-2. Virsmas raupjuma mērīšanas eksperimenti ar 11 virsmām rāda, ka mēraparāta soļa vērtības virsmas garenvirzienā nav ticamas, sakarā ar virsmas vidējās plaknes un profila viduslīnijas nesakrišanu. Veicot papildus aprēķinus tika secināts, ka parametru Str var pielietot raupjuma anizotropijas novērtēšanai, piemēram, slīpētām, pulētām, berzes virsmām un citām virsmām ar līdzīgām īpašībām.

12.12.2016.

DOI: 10.1515/lpts-2017-0013

THEORETICAL ANALYSIS OF SPACING PARAMETERS OF
ANISOTROPIC 3D SURFACE ROUGHNESS

J.Rudzitis, N.Bulaha, J.Lungevics, O.Linins, K.Berzins

Institute of Mechanical Engineering,

Riga Technical University,

6 Ezermalas Str., LV-1006, Riga, LATVIA

e-mail: mti@rtu.lv

The authors of the research have analysed spacing parameters of anisotropic 3D surface roughness crosswise to machining (friction) traces RSm_1 and lengthwise to machining (friction) traces RSm_2 . The main issue arises from the RSm_2 values being limited by values of sampling length l in the measuring devices; however, on many occasions RSm_2 values can exceed l values. Therefore, the mean spacing values of profile irregularities in the longitudinal direction in many cases are not reliable and they should be determined by another method. Theoretically, it is proved that anisotropic surface roughness anisotropy coefficient $c=RSm_1/RSm_2$ equals texture aspect ratio Str , which is determined by surface texture standard EN ISO 25178-2. This allows using parameter Str to determine mean spacing of profile irregularities and estimate roughness anisotropy.

Keywords: *anisotropy coefficient, roughness spacing parameters, surface texture, texture aspect ratio.*

1. INTRODUCTION

As a result of introducing surface texture standard (EN ISO 25178-2) [1], interest in 3D surface roughness parameters is growing. Knowing spacing parameters of the 3D surface roughness, especially if surface roughness is anisotropic, is an important factor in solving different technical tasks (friction, wear, part contacting etc.).

Surface roughness is anisotropic if in different surface directions profiles are different, unlike isotropic surface roughness that has the same profiles in all directions.

The main interest lies in surfaces with anisotropy in mutually perpendicular directions. In such a case, roughness mean spacing of profile irregularities is as follows: RSm_1 – crosswise to machining (friction) traces and RSm_2 – lengthwise to machining (friction) traces (Fig. 1).

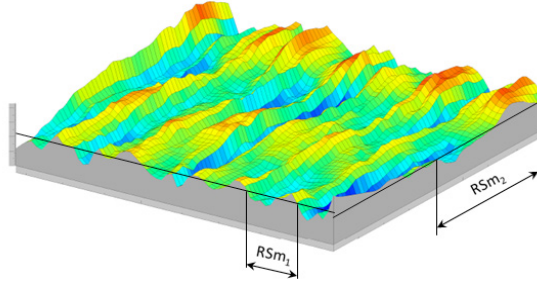


Fig. 1. Example of 3D surface with anisotropic roughness.

Engineering tasks require that the spacing parameters be easily identifiable and technologically feasible in machining. Otherwise, these parameters have no practical value.

In standard EN ISO 4287 [2], spacing parameter RSm is defined as mean width of profile elements along the mean line of the profile.

However, the ratio between spacing parameters RSm_1 and RSm_2 , which characterises the anisotropy of surface roughness, is not defined in standards. Yet it is an important value that is required for characterising surface anisotropy and is used by surface scientists [5]–[10].

Based on the uniformed surface characterisation, the control bases of these parameters – mean lines – should be located at the level of the mean plane of rough surface (Fig. 2). Then these spacing parameters characterise a 3D surface.

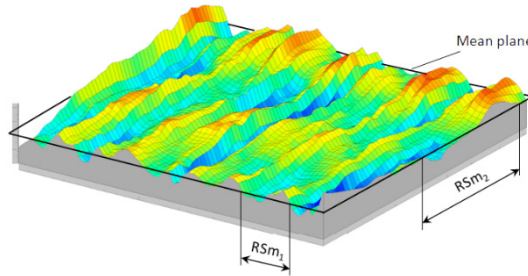


Fig. 2. Placement scheme of 3D surface roughness spacing parameters.

The authors of the paper have designated the ratio between spacing parameters as c :

$$c = \frac{RSm_1}{RSm_2}. \quad (1)$$

Parameter c is identified as an anisotropy coefficient. If surface is *isotropic*, $RSm_1=RSm_2$ and $c=1$. However, if surface is anisotropic, $RSm_2 \rightarrow \infty$, $c \rightarrow 0$.

Current 3D surface roughness measurement devices, for instance, Taylor Hobson Intra 50, identify the spacing parameters without linking the mean line of the profile with the mean plane of the surface. This results in significantly lower RSm

values and notably influences parameter RSm_2 . This can be clearly seen in Fig. 3, which shows values of parameters Sa , RSm_1 and RSm_2 of a grinded surface with irregular surface roughness (Sa – arithmetic mean height of the scale limited surface). Surface roughness measurements that are used in this paper hereinafter were obtained using Taylor Hobson measuring equipment Intra 50.

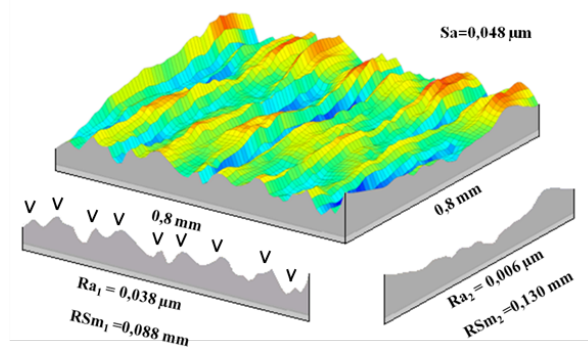


Fig. 3. Parameter values of grinded surface.

3D surface roughness parameter for the grinded surface shown in Fig. 3 is $Sa=0.048 \mu\text{m}$, and this parameter is identified as a deviation from the roughness mean plane. If the mean plane is also crossed by roughness sections (profiles), profile arithmetic mean deviation value Ra should be close to the 3D surface value Sa (in theory, at infinite number of profiles $Ra \rightarrow Sa$).

In the given example (Fig. 3), surface roughness in crosswise direction is $Ra_1=0.038 \mu\text{m}$, which is close to $Sa=0.048 \mu\text{m}$. Thus, it can be assumed that the mean line of crosswise profile of surface roughness is closely positioned to surface roughness mean plane. Thus, the mean spacing of profile irregularities RSm_1 can be assumed as a value of the crosswise mean spacing of profile irregularities belonging to the 3D surface roughness, and in this case $RSm_1=0.088 \text{ mm}$. It can be clearly seen from the form of the crosswise profile (Fig. 3). The profile in question has 9 visible irregularities (Fig. 3, marked with a tick) along the evaluation length $L=0.8 \text{ mm}$ enabling one to approximately estimate that $RSm_1 \approx L/9 = 0.8/9 = 0.089 \text{ mm}$. This value is close to the value determined by the measuring equipment, i.e., $RSm_1=0.088 \text{ mm}$. Hereinafter, such a way of determining spacing parameters will be called the *visual* determination method.

This method will also be used for other surface profiles that are given reduced values of mean spacing of profile irregularities by the measuring equipment comparing to the real values.

The example (Fig. 3) shows a slightly different situation regarding surface roughness in longitudinal direction, with $Ra_2=0.006 \mu\text{m}$ substantially differing from $Sa=0.048 \mu\text{m}$. This shows that the mean line of the longitudinal profile of surface roughness is distant from the mean plane of surface roughness, and the mean value of the mean spacing of profile irregularities is $RSm_2=0.130 \text{ mm}$, which is not accurate and does not characterise surface anisotropy correctly. This value cannot be used in formula (1) to determine anisotropy coefficient c . The visual method, in turn,

allows one to determine RSm_2 value more accurately. The profile in question has approximately 2 irregularities along the evaluation length $L=0.8$ mm. Consequently, $RSm_2 \approx L/2 = 0.8/2 = 0.4$ mm, which is approximately 3 times the value determined by the measuring equipment, i.e., $RSm_2 = 0.130$ mm. It can be seen with unaided eye that this value is more probable (Fig. 3).

It can be concluded that there is a big difference in the results depending on whether the values of mean spacing of profile irregularities RSm_2 (surface in Fig. 3) were measured with measuring equipment or using the visual determination method.

How to determine the value of 3D surface parameter RSm_2 ? Apparently, one can use parameter Str – a texture aspect ratio provided in standard EN ISO 25178-2.

2. TEXTURE ASPECT RATIO

According to American National Standard ASME B46.1-2009 “Surface Texture” [4] and [3]:

$$Str = \frac{L_F}{L_{Sl}}, \quad (2)$$

where L_F – length of the fastest decay of ACF;

L_{Sl} – length of the slowest decay of ACF;

ACF – the autocorrelation function.

Mathematical expression of ACF between two points with coordinates $(x_1; y_1)$ and $(x_2; y_2)$ can be written as $\rho(\tau_1; \tau_2)$, where $\tau_1 = x_2 - x_1$ – distance between points on axis x and $\tau_2 = y_2 - y_1$ – distance between points on axis y . When the distance between the points increases (by increase of values τ_1 and τ_2), values $\rho(\tau_1; \tau_2)$ decrease (Fig. 4).

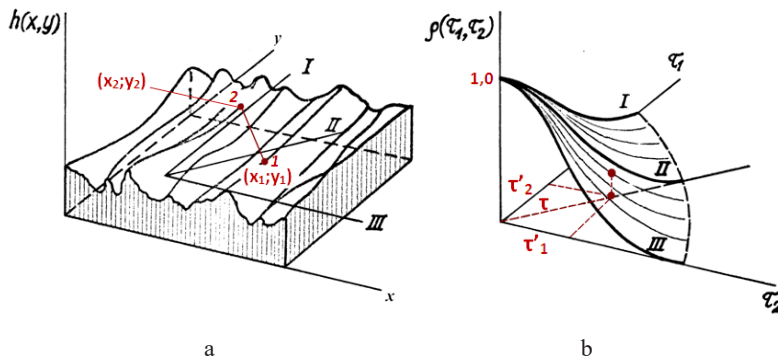


Fig. 4. Schematic representation of surface roughness (a) and corresponding standardised correlation function (b) [7].

Decrease rate of values of the correlation function can be characterised by correlation interval τ_k , which for the particular section is determined as follows:

$$\tau_k = \int_0^{\infty} |\rho(\tau)| d\tau, \quad (3)$$

where $\rho(\tau)$ – the autocorrelation function of surface roughness section.

Geometrically, τ_k is length of an edge of a rectangular base, the other edge of which is 1 and the area is equal to an area of a standardized correlation function under the curve. Value of τ_k for surface depends on the properties of the section.

In case of anisotropic surface roughness, the surface correlation function can be placed differently towards axes x, y (Fig. 5).

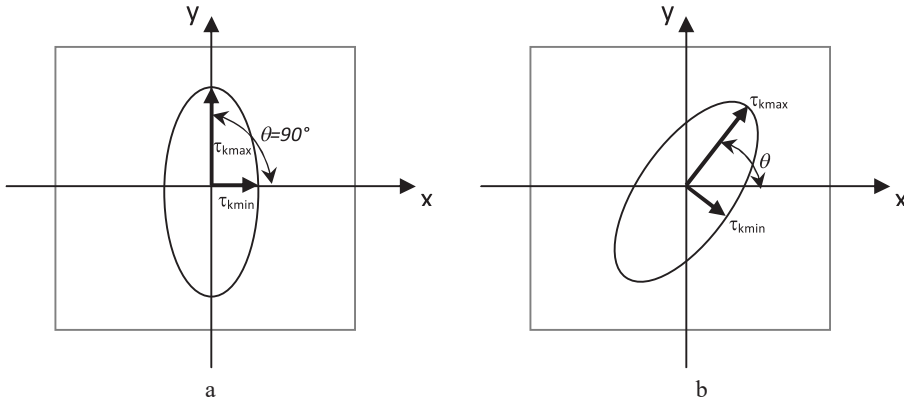


Fig. 5. Schematic placement of τ_k [1]

a – the correlation function is oriented along axes x and y, b – the correlation function is not oriented along axes x and y.

Assuming that the correlation function $\rho(\tau_1; \tau_2)$ is oriented along base-directions of anisotropic rough surface: τ_1 axis along direction x, τ_2 axis along direction y. This means that $L_F = \tau_{kmin} = \tau_{kx}$, but $L_{Sl} = \tau_{kmax} = \tau_{ky}$ because the surface profile has greater irregularity density crosswise to machining (friction) traces and the correlation function is descending faster as well. Thus, according to formula (2), it can be represented as follows:

$$Str = \frac{\tau_{kx}}{\tau_{ky}}. \quad (4)$$

It should be noted that standard EN ISO 25178-2 [1] foresees that the autocorrelation function is determined at level $0 \leq s \leq 1$ (usually $s=0.2$). However, at any level of s , ratio (4) retains its basic value; therefore, formula (4) can be used to characterise parameter Str at any s value, without losing the general approach.

Using studies on correlation functions of profiles of irregular rough surfaces [7], for a monotonically decreasing function:

$$\tau_k = \frac{\tau_{kn}}{E\{n(0)\}}, \quad (5)$$

where τ_{kn} – the standardised value of the correlation interval. It is constant for the particular correlation function.

$E\{n(0)\}$ – mathematical expectation of intersections with the mean line of the roughness profile (zero count).

In accordance with formula (4) for the particular correlation function:

$$Str = \frac{E\{n_2(0)\}}{E\{n_1(0)\}}, \quad (6)$$

where indices 1 and 2 characterise crosswise and longitudinal profiles, respectively. Since $E\{n(0)\}=2/RSm$ [7], then:

$$Str = \frac{RSm_1}{RSm_2}. \quad (7)$$

Comparing the obtained formula (7) with (1), one gets important data for determining surface anisotropy coefficient c :

$$Str = c. \quad (8)$$

This means that the correlation function, which is orientated along the surface directions, allows using parameter Str to determine anisotropic coefficient c .

3. RSm_2 DETERMINATION

Using oriented correlation function of surface roughness in accordance with formula (8), RSm_2 value can be easily determined:

$$RSm_2 = \frac{RSm_1}{Str}, \quad (9)$$

where parameter Str is determined with the corresponding measuring equipment, such as Taylor Hobson Intra 50.

In general situations, when there are no notable mutually perpendicular base-directions of surface roughness, formulas (7), (8), (9) cannot be applied, for instance, for a cylinder liner of an internal combustion engine machined by honing operation.

There is another way to determine RSm_2 .

Random field theory, which allows connecting 3D surface parameters with engineering tasks (surface contact, friction, wear etc.), is becoming increasingly popular in the modelling of irregular surface roughness (abrasion, worn surfaces etc.) [6], [7], [8].

If surface roughness is described with a random field, using theory of normal random field [10]:

$$E^2\{n_\phi(0)\} + E^2\{n_{\phi+90^\circ}(0)\} = \text{const}, \quad (10)$$

where $n_\phi(0)$ – the number of zeroes of section at angle ϕ of normal random field (number of intersections between the profile and mean line);

$n_{\phi+90^\circ}(0)$ – the number of zeroes of section at angle $\phi+90^\circ$ of normal random field;

$E\{\}$ – mathematical expectation of random variable.

According to the given formula, sum of squares of zeroes of any 2 mutually perpendicular sections is constant. Consequently, it can be written as follows:

$$E^2\{n_{0^\circ}(0)\} + E^2\{n_{90^\circ}(0)\} = E^2\{n_{45^\circ}(0)\} + E^2\{n_{135^\circ}(0)\} \quad (11)$$

Assuming that section at $\phi=0^\circ$ is the first direction (in the direction of axis x) and $\phi=90^\circ$ is the second direction (in the direction of axis y), formula (11) can be simplified:

$$E^2\{n_1(0)\} + E^2\{n_2(0)\} = E^2\{n_{45^\circ}(0)\} + E^2\{n_{135^\circ}(0)\} \quad (12)$$

If the profiles are taken at $\phi=45^\circ$ and 135° , the number of zeroes is the same:

$$E^2\{n_{45^\circ}(0)\} = E^2\{n_{135^\circ}(0)\} \quad (13)$$

From expressions (12), (13) it can be concluded that:

$$E^2\{n_2(0)\} = 2 \cdot E^2\{n_{45^\circ}(0)\} - E^2\{n_1(0)\}. \quad (14)$$

Dividing both sides by $E^2\{n_1(0)\}$, one gets:

$$c^2 = 2 \cdot \left[\frac{E\{n_{45^\circ}(0)\}}{E\{n_1(0)\}} \right]^2 - 1, \quad (15)$$

where c – the anisotropy coefficient (see (1)).

$$c = \frac{E\{n_2(0)\}}{E\{n_1(0)\}} = \frac{E\{RSm_1\}}{E\{RSm_2\}}. \quad (16)$$

Using formula (1),

$$RSm_2 = \frac{RSm_1}{c}. \quad (17)$$

It should be noted that this approach has two disadvantages:

- 1) a need for additional information to determine $n_{45^\circ}(0)$;
- 2) the method is limited by expression (15) that determines the following:

$$\frac{\sqrt{2}}{2} \leq \frac{E\{n_{45^\circ}(0)\}}{E\{n_1(0)\}} \leq 1.0. \quad (18)$$

If the experimental values $n_1(0)$ and $n_{45^\circ}(0)$ do not result in formula (18), parameter RSm_2 should be obtained applying the *visual* method (see paragraph 1).

It should be taken into account that the suggested RSm_2 determination method significantly differs from the classical surface roughness metrology if surface roughness is anisotropic. In compliance with the classical metrology, all surface roughness parameters are determined within the limits of sampling length l [2]. However, in the given approach, using formulas (9) and (17), RSm_2 values can even exceed sampling length l , which is selected according to the value of parameter Ra (see Table 2).

In classical metrology, such RSm_2 values could be viewed as waviness mean spacing; however, mean spacing of profile elements RSm_1 and RSm_2 essentially characterise one but very longitudinally stretched irregularity, which has formed due to friction, wear, grinding or any other similar process. Physically, it is not linked to waviness.

Consequently, this RSm_2 value should be used in friction-, wear- and other technical calculations where mean spacing of profile elements for surface roughness has to be taken into account.

4. CONCLUSIONS

Within the framework of the research, the authors have evaluated anisotropy of surface roughness. First of all, the mean spacing values of profile irregularities obtained by measuring equipment have been analysed for flat grinded surface. It has been stated that mean spacing values of profile irregularities in longitudinal direction are not reliable due to the fact that surface mean plane and profile mean line are located at different levels. In addition, for the initial determination of roughness of mean spacing of profile irregularities RSm_2 the visual method has been proposed. Secondly, anisotropy coefficient c and surface texture aspect ratio Str have been compared. During the theoretical study, it has been substantiated by formulas that surface texture parameter Str , which is standardised in ISO 25178-2:2012, can be used to evaluate roughness anisotropy and calculate spacing parameters.

REFERENCES

1. International Organisation for Standardisation, (2012). Geometrical product specifications (GPS) – Surface texture: Areal – Part 2: Terms, definitions and surface texture parameters. ISO 25178-2:2012.
2. International Organisation for Standardisation (1997). Geometrical Product Specifications (GPS) – Surface texture: Profile method – Terms, definitions and surface texture parameters. ISO 4287:1997.
3. Stout, K.J. (2000). *Development of Methods for Characterisation of Roughness in Three Dimensions*. London: Penton Press.
4. American Society of Mechanical Engineers (2009). Surface Texture (Surface Roughness, Waviness, and Lay). ASME B46.1-2009.
5. Nayak, P. (1971). Random Process Model of Rough Surfaces. *Journal of Lubrication Technology*, 93(3), 398–407.
6. Rudzitis, J. (2007). *Mechanics of Surface Contact. Part 1. Parameters of Surface Roughness pProfile*. Riga: Riga Technical University (in Russian).
7. Kumermanis, M. (2012). *Research of 3D Roughness Parameters for Irregular Surfaces of Solid Bodies*. Riga: Riga Technical University (in Latvian).
8. Linins, O., Boiko, I., Lungevics, J., & Leitans, A. (2016). New Methodology for the Life Time Prediction of Wear Parts in the Mechatronic Systems. In *12th International Conference "MSM Systems"*, 3 – 8 July 2016 (pp.122–122). Bialystok, Poland: Bialystok University of Technology.
9. Kragelsky, I.V. (1982). *Friction Wear Lubrication. Tribology Handbook* (Vol. 1). Moscow: Mir Publishers.
10. Longuet-Higgins, M.S. (1957). Statistical properties of an isotropic random surface. *Philosophical Transactions of the Royal Society of London. Series A, Mathematical and Physical Sciences*, 250(975), 157–174.

ANIZOTROPĀ 3D VIRSMAS RAUPJUMA SOĻA PARAMETRU TEORĒTISKĀ ANALĪZE

J.Rudzitis, N.Bulaha, J.Lungevičs, O.Liniņš, K.Bērziņš

Kopsavilkums

Dotajā zinātniskajā darbā veikta anizotropiska 3D virsmas raupjuma soļa parametru analīze, šķērsām apstrādes (berzes) pēdām RSm_l un paralēli apstrādes (berzes) pēdām RSm_z . Problēmas būtība ir tā, ka RSm_z vērtības mēraparātos ir ierobežotas ar bāzes garuma l vērtībām, kaut gan vairākos gadījumos virsmas RSm_z vērtības var pārsniegt l vērtības. Tāpēc arī soļa parametra vērtības garenvirzienā vairākos gadījumos nav ticamas un tās ir jānosaka ar citu paņēmieni. Teorētiski ir pierādīts, ka anizotropa virsmas raupjuma gadījumā anizotropijas koeficients $c=RSm_l/RSm_z$ ir vienāds ar virsmas tekstūras indeksu Str , kuru nosaka virsmas tekstūras standarts EN ISO 25178-2. Sakarā ar to, parametru Str ir iespēja pielietot raupjuma soļu noteikšanai un raupjuma anizotropijas novērtēšanai.

12.07.2016.

TRIBOLOGICAL PROPERTIES OF PVD Ti/C-N NANOCOATINGS

A. Leitans, J. Lungevics, J. Rudzitis, A. Filipovs
Institute of Mechanical Engineering,
Riga Technical University,
6 Ezermalas Str., LV-1006, Riga, LATVIA
e-mail: mti@rtu.lv

The present paper discusses and analyses tribological properties of various coatings that increase surface wear resistance. Four Ti/C-N nanocoatings with different coating deposition settings are analysed. Tribological and metrological tests on the samples are performed: 2D and 3D parameters of the surface roughness are measured with modern profilometer, and friction coefficient is measured with *CSM Instruments* equipment. Roughness parameters Ra, Sa, Sz, Str, Sds, Vmp, Vmc and friction coefficient at 6N load are determined during the experiment. The examined samples have many pores, which is the main reason for relatively large values of roughness parameter. A slight wear is identified in all four samples as well; its friction coefficient values range from 0.21 to 0.29. Wear rate values are not calculated for the investigated coatings, as no expressed tribotracks are detected on the coating surface.

Keywords: *magnetron deposition, nanocoatings, roughness, wear resistance.*

1. INTRODUCTION

The wear of elements in the mechanical engineering sector is a topical problem, which is associated with the reduction of actuating mechanism life span and the decrease of efficient performance. As it is known, when two components contact with each other, the friction forces between the surfaces emerge both during component slip and rotation movements. Therefore, the presence of friction significantly reduces the energy efficiency of the mechanism, efficiency as such, as well as end-product quality.

In order to reduce friction and ensure high wear resistance, coatings obtained from magnetron deposition technology are applied; their main advantages are the conservation and biochemical functionality of substrate material properties. Such coatings evenly adhere to the substrate and are free from micro cracks. The coatings of Ti/C-N type have a high level of surface adhesion when applied to the component, ensuring the provision of a minimum friction coefficient obtained in contact with another component. These types of coating also have both high micro hardness and

high permissible operating temperatures [1], [4].

2. PREPARING SUBSTRATES FOR DEPOSITION EXPERIMENT

The substrate material is chrome steel 100Cr6 according to DIN 17230:1980; round samples with a diameter of 18 mm served as substrates. Prior to the deposition procedure, all samples were subject to ultrasonic cleaning using “Lotonaxe” degreasing bath, then cleaning in water-alcohol solution was performed and drying with hot air was carried out. After that, when the experimental samples were fixed and put in the chamber, the substrate surface was activated in argon atmosphere using ion beam equipment.

Deposition equipment VU-VSM 600/4 was used in order to perform Ti/C-N coating deposition. Deposition process was implemented following a satellite method, i.e., magnetron horizontally opposite location was used during the deposition time.

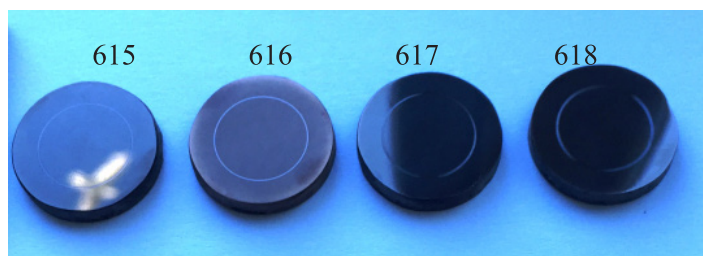


Fig. 1. Samples with Ti/C-N coating.

During deposition, sample No. 615 had the highest rotational speed; subsequently, smaller nanolayers were deposited. Sample No. 616 had higher TiN concentration, but sample No. 618 was the closest to the targets.

Table 1

Cu/C Coating Deposition Regimes

No.	Nanostructured coating	Density, μm	Sample rotation degree	Distance from magnetron to component, mm	Carousel rotation speed, rpm
1	615	3.9	2	100	3
2	616	4.2	2	100	2
3	617	3.9	2	100	2
4	618	3	2	60	2

3. EXPERIMENTAL PART

To assess exploitation qualities of Ti/C-N surface coatings, it is important to analyse the surface topography and 2D and 3D roughness parameters, as well as the friction coefficient values and wear intensity.

Modern measuring equipment Taylor Hobson Intra 50 was used for roughness measuring experiments. It belongs to a profilometer group of contact type measurement methods, which means that the machine is scanning the studied surface directly sliding over it with a thin hard metal needle *Standard Stylus Arm 112/2009*, which has a peak rounding radius of $2\mu\text{m}$ and pressure force on the studied surface of 1mn , thus obtaining information on actual surface roughness character, i.e., profile chart.

During the experiment, measurement process settings were defined:

- individual profile chart length (X-axis) – 2 mm ;
- measured point number on each individual profile chart – 400 points;
- parallel profile chart number – 400 pieces;
- needle movement speed on X-axis – 0.5 mm/s .

In the performed experiments, a $2\text{x}2\text{mm}$ large sample surface fragment was explored. There were 400 mutually parallel profile chart measurements taken within the investigated fragment. 400 points that characterise the surface profile were displayed in each profile chart obtained. Overall, for a $2\text{x}2\text{mm}$ large working area, a measurement matrix with $160,000$ points was obtained, from which the equipment software formed a 3D surface image, which was then subjected to filtering operations in order to get a real surface topography.

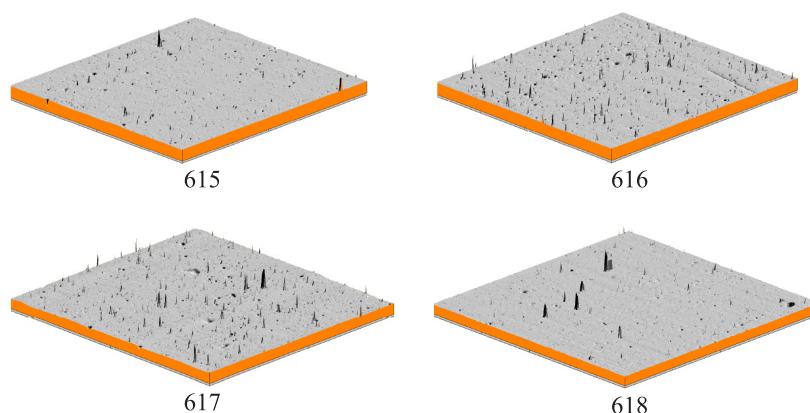


Fig. 2. 3D photo simulations of Ti/C-N naocoating.

Table 2 summarises 2D surface roughness (Ra) and 3D (Sa, Sz, Sds, Str) parameters [3].

Table 2

Overview of 2D and 3D Measurement Results

Sample	Ra	Sa	Sz	Sds	Str	Vmp	Vmc
	(μm)	(μm)	(μm)	(pks/mm^2)		(mm^3/mm^2)	(mm^3/mm^2)
615	0.0263	0.0239	4.29	1644	0.693	2.41E-04	1.97E-03
616	0.0385	0.0262	4.3	1813	0.62	2.35E-04	1.75E-03
617	0.0349	0.0391	5.16	2055	0.5	2.25E-04	1.60E-03
618	0.0224	0.028	4.55	1585	0.67	8.91E-05	6.59E-04

The received data allow concluding that the samples have a substantial amount of pores, which also serve as the main reason for relatively large values of roughness parameter (see Table 2). Although the coatings as such are completely isotropic, their isotropy Str characterising parameter value does not exceed 0.69, which is explained by the fact that the coatings copy substrate surfaces with pronounced surface treatment direction, i.e., surfaces are anisotropic.

To obtain information on tribological properties of the samples studied in the article, friction coefficient measurements of all four investigated samples No. 615, 616, 617, 618 were taken [2]. The present slip friction experiments were carried out using *CSM Instruments* tribometer, following the ball-on-disc scheme (see Fig. 3), where the disk was represented with the sample substrate with the coating, which was rotating, while the ball was a stationary tribometer element. This method complies with ASTM G99 tribology test standard. Experiment settings can be observed in Table 3.

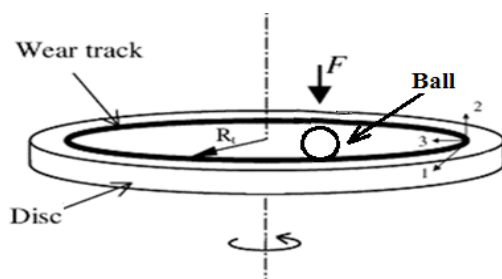


Fig. 3. “Ball-on-disc” test equipment scheme.

Table 3

Experiment Settings

<i>Tracking force</i>	6 N
<i>Sample rotation number</i>	1500 cycles
<i>Linear speed of friction pair</i>	0.05 m/s
<i>Tribological track radius</i>	6 mm
<i>Ball diameter</i>	6 mm
<i>Ball material</i>	100Cr6 (EN)
<i>Surface cleaning</i>	Alcohol solution
<i>Atmosphere</i>	Air
<i>Temperature</i>	22 °C (indoors)
<i>Humidity</i>	40 % (indoors)

To gain information on wear resistance of the studied sample, wear resistance experiments were carried out, which resulted in getting wear tracks – tribological tracks. To evaluate the wear resistance of the samples, it is necessary to know cross-sectional areas of tribological track. The parameter which is of interest may be obtained using contact type Surtronic 25 profilometer and, if necessary (in case the cross-sectional area of tribological track is very small), via Intra 50.

The measurements were carried out following the provided algorithm:

1. the studied sample was placed on the profilometer table;
2. three independent cross-sectional area measurements with the following profilometer settings were performed:
 - measurement track length $l_t = 1\text{mm}$;
 - resolution range (for Surtronic 25 profilometer) – $10\mu\text{m}$.

Figure 4 shows measurement positioning on the sample:

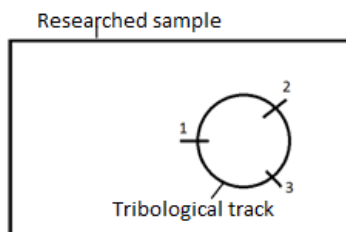


Fig. 4. Positioning of cross-sectional measurement of tribological track on the sample.

1. the profile chart post-treatment was performed, following the provided algorithm:
 - making profile chart levelling by means of *Leveling* tool;
 - bringing closer the profile chart part, which was of interest, using *Zoom* function;
 - calculating the cross-sectional area of tribological track via *Surface of a Hole/Peak* function.
2. the average value of tribological track cross-sectional area was calculated. This value was used for further calculations.

4. RESULTS AND DISCUSSION

Figure 5 shows the coefficient of friction curve of the studied sample. The data were obtained performing measurements with the settings presented in Table 4.

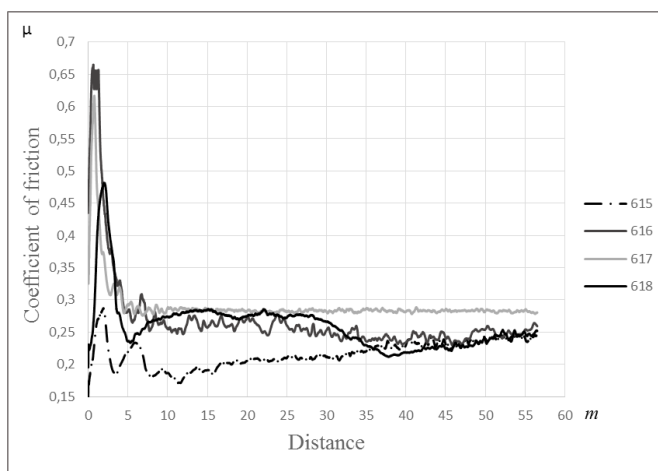


Fig. 5. Summative graph of friction coefficient curves of the studied sample.

Table 4

Average Values of Friction Coefficient

Sample	COF
615	0.217
616	0.27
617	0.291
618	0.261

Table 4 shows the average values of friction coefficient of the studied samples. Slight wear of the examined samples was detected, the tribotrack of which could not be accurately measured with Surtronic-25 profilometer. Therefore, the measurements were carried out with profilometer Intra 50. In the measured tribological track area of 615, 617 and 618 coatings, a rough surface without the expressed tribological track area was discovered. Figures 6 and 7 serve as an example of it. Out of four examined samples, in case of 616 coatings, tribological track (around $0.4\mu\text{m}$ depth and $0.2\mu\text{m}$ width) was identified (see Figure 9), which also indicated unnoticeable wear at the given experimental conditions; the coating thickness of the sample 616 was $4.2\mu\text{m}$.

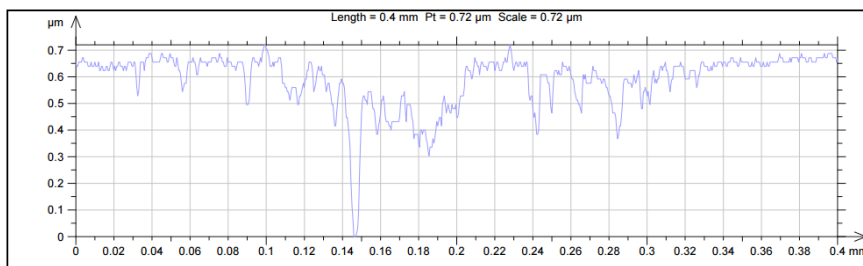


Fig. 6. Tribological track of sample 615.

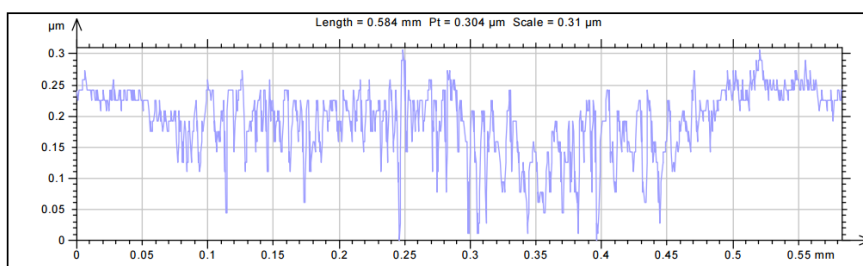


Fig. 7. Tribological track of sample 617.

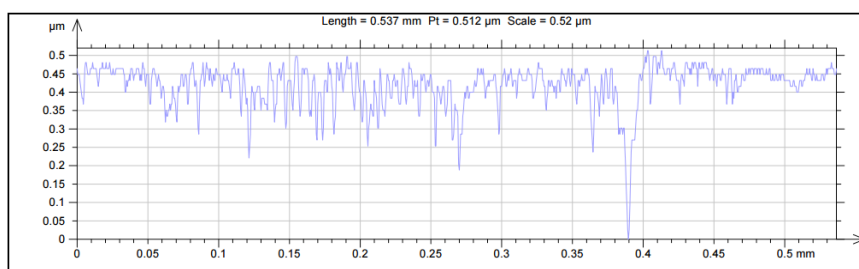


Fig. 8. Tribological track of sample 618.

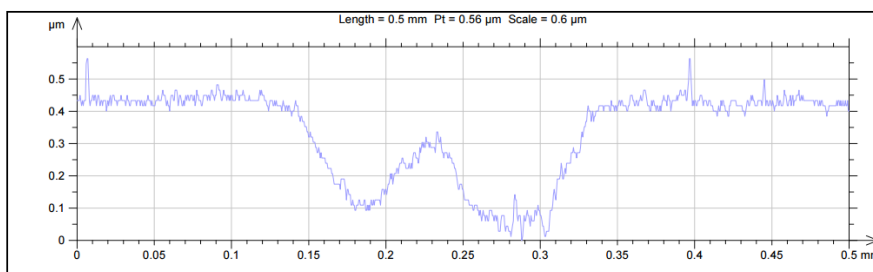


Fig. 9. Tribological track of sample 616.

Due to the absence of expressed tribological tracks, the wear rate values were not calculated for three out of the four investigated coatings.

5. CONCLUSIONS

Within the framework of the present research, it has been stated that the Ti/C-N coatings have a lot of pores, so it is the main reason for large values of roughness parameters. In all four samples, slight wear has been detected. Coefficient of friction values range from 0.21 to 0.29. The sample 615 has the lowest value of friction coefficient obtained under certain conditions, which can be observed in common deposition mode setting table. Wear rate values have not been calculated for the investigated coatings, as no expressed tribotacks have been detected on the coating surface.

ACKNOWLEDGEMENTS

The present research has been supported by the European Regional Development Fund within the project No.2014/0011/2DP/2.1.1.1.0/13/APIA/VIAA/005.

REFERENCES

1. Cheng, Y., & Zheng, Y.F. (2007). Characterization of TiN, TiC and TiCN coatings on Ti-50.6 at.% Ni alloy deposited by PIII and deposition technique. *Surface and Coatings Technology*, 201(9-11), 4909-4912.
2. CSM Instruments SA. (2014). *Tribometer User Manual R0.1.3a*.
3. International Organisation for Standardisation. (2012). LVS EN ISO 25178-2:2012 standard: Geometrical product specifications (GPS) – Surface texture: Areal - Part 2: Terms, definitions and surface texture parameters.
4. Локтев Д., Ямашкин Е. (2007). Основные виды износостойких покрытий. *Наноиндустрия*, №5, 24-30.

PVD Ti/C-N NANOPĀRKLĀJUMU TRIBOLOĢISKĀS ĪPAŠĪBAS

A.Leitans, J.Lungevičs, J.Rudzītis, A.Ļipovs

Kopsavilkums

Šajā darbā tika apskatīta un analizēta dažādu pārklājumu, kas palielina virsmu nodilumizturību, triboloģiskās īpašības. Tika analizēti četri Ti/C-N nanopārklājumi, kuri atšķiras ar pārklājuma uznešanas uzstādījumiem. Pētāmiem paraugiem tika veikti metroloģiskie un triboloģiskie testi: tika nomērīti virsmas raupjuma 2D un 3D parametri ar moderno profilogrāfu-profilometru un berzes koeficients ar *CSM Instruments* firmas iekārtu. Pārbaudes eksperimentu laikā tika noteikti raupjuma parametri Ra, Sa, Sz, Str, Sds, Vmp, Vmc un berzes koeficients pie 6N slodzes. Pētāmiem paraugiem ir daudz poru, kas ir galvenais iemesls salīdzinoši lielajām raupjuma parametru vērtībām. Kā arī tika konstatēts neliels nodilums visiem četriem paraugiem; To berzes koeficientu vērtības svārstās robežās 0,21-0,29. Pētāmajiem pārklājumiem netika aprēķinātas nodiluma rādītāja vērtības, jo izteikti tribotreki uz pārklājuma virsmas nebija konstatēti.

20.07.2016.



BALTIC FLOWS

PROJEKTA BALTIC FLOWS REZULTĀTI

A. Kalnačs

Fizikālās enerģētikas institūts

Krīvu iela 11, Rīga, LV-1006, LATVIJA

2016. gadā, piedaloties arī trīs organizācijām no Latvijas, tika pabeigts Eiropas Savienības 7. ietvarprogrammas projekts Baltic Flows. Lasītāju iepazīstināšana ar projektu un tā organizāciju jau ir veikta agrākā šī žurnāla numurā (skat. 2016. g. oktobrī izdoto numuru N5). Šajā īsajā ziņojumā ir uzskaitīti visi 8 galvenie projektā izstrādātie un tā rezultātus aprakstošie dokumenti. Par katru no dokumentiem dots ļoti konspektīvs apraksts. Vairāk informācijas par projektu un šeit aprakstīto dokumentu pilni oriģināli anglu valodā ir atrodami projekta interneta vietnē www.balticflows.eu. Pirms katra dokumenta nosaukuma šajā rakstā ir dots tā kods, pēc kura iespējams precīzi identificēt dokumenta angļu versiju minētajā interneta vietnē.

D3.3 Analīze reģionu potenciālam pilsētvides lietusgāzu ūdeņu apsaimniekošanā. Viens no projekta mērķiem ir apkopot un analizēt labākās prakses piemērus lietusgāzu ūdeņu pārvaldībā blīvi apdzīvotās teritorijās. Līdz ar to viens no projekta uzdevumiem bija novērtēt iespējas ieviest minētās labākās prakses arī citās vietās un reģionos. Tas tika veikts, analizējot veiksmes faktorus un to darbības principus lietusgāzu ūdeņu pārvaldībā. Šī darba galvenais mērķis ir apkopot darbu rezultātus un iegūtās zināšanas aprakstītajās jomās, kā arī identificēt, kuriem reģioniem ir nepieciešama palīdzība.

D3.4 Pētījums par pilsētvides miniatūro lietus ūdens monitoringa tehnoloģiju pieprasījumu un izaicinājumiem. Šis ziņojums izklāsta tirgus iespējas Eiropā par tā virsrakstā minētajām tehnoloģijām. Tāpat ziņojums apraksta izaicinājumus, ko risina gan esošās, gan arī izstrādē esošās tehnoloģijas tā jomā. Ir sniegts plašs, bet ne izsmelošs instrumentu un tehnoloģiju saraksts. Dokumenta nobeigumā dots pilsētvides ūdens monitoringa tehnoloģiju apskats.

D3.6 Jaunākās zināšanas lietusgāzu ūdeņu apsaimniekošanai pilsētvidē. Urbanizācija un ar to saistītā arvien lielāku laukumu noklāšana ar ūdensnecaurlaidīgiem materiāliem (asfalts, betons, u.tml.) turpina palielināt plūdu, ūdensapgādes traucējumu un piesārņojuma riskus pilsētās un to tuvumā esošās

ūdenskrātuvēs. Šis ziņojums sniedz plašu apskatu par labāko praksi un zināšanām lietusgāžu ūdeņu apsaimniekošanai pilsētvidē Baltijas jūras reģionā. Tas dod lasītājiem jaunas zināšanas lietusgāžu ūdeņu apsaimniekošanai pilsētvidē un sniedz rekomendācijas tālākai ekonomiskai, tehniskai un vides attīstībai.

D4.2 Iedzīvotāju iesaiste ūdens monitoringā – kā to veicināt? Tehnoloģisko risinājumu miniaturizācija un izmaksu samazināšanās, kā arī sociālo tīklu un citas informācijas tehnoloģijas ir padarījušas iespējamu ūdens resursu uzraudzību ar brīvprātīgu iedzīvotāju palīdzību. Rezultātā ir iespējama detalizēta un nepārtraukta gan kvantitatīva (plūdu riski), gan kvalitatīva (piesārņojums) ūdens resursu uzraudzība. Šajā ziņojumā ir apkopti projektā veikto aptauju rezultāti par iedzīvotāju velmi un motivāciju iesaistīties ūdens monitoringā, kā arī apskatīti tehnoloģiskie risinājumi, **kā to iespējams veikt. Apkopota arī labākā projekta dalībvalstu pieredze, kurā Latvijas valsts vides dienesta publisko inspektoru programma ir atzīta, kā viena no divām inovatīvākajām identificētajām programmām iedzīvotāju iesaistīšanā vides novērojumos.**

D5.3 Analīze reģionu potenciālam izkliegtā piesārņojuma monitoringā. Šis ziņojums satur analīzi par viedās specializācijas potenciālu ūdens kvalitātes monitoringā projektā iesaistītajās valstīs. Tajā aprakstīts, kādus risinājumus minētās valstis var piedāvāt gan pārējai Eiropai, gan globāli. Ziņojumā aprakstītas arī pašreizējās ūdens kvalitātes novērošanas vajadzības, pieprasījums pasaulē un problēmas. Īpaša vērība tiek pievērsta tieši izkliegtā piesārņojuma novērošanai.

D5.4 Pētījums par strautu un upju miniatūro ūdens monitoringa tehnoloģiju pieprasījumu un izaicinājumiem. Pašreiz lietotās ūdens monitoringa metodes, kas balstās uz gadījuma rakstura paraugu ņemšanu manuālām datu pārvaldības metodēm un ierobežotu dārgu nepārtrauktās uzraudzības ierīču lietošanu, nedod iespēju nepārtraukti uzraudzīt lielas ģeogrāfiskās platības un ūdens plūsmas ar izkliegtā piesārņojumu. Šajā ziņojumā ir apskatītas iespējas, izaicinājumi, un problēmas pārejai no esošajām ūdens kvalitātes monitoringa tehnoloģijām uz jaunu ēru šajā jomā iezīmējošām autonomām mazu izmaksu ūdens monitoringa sistēmām.

D5.6 Jaunākās zināšanas izkliegtā piesārņojuma uzraudzībā – pašreizējās situācijas apskats. Šajā ziņojumā tiek apskatīts izkliegtā piesārņojuma (t.i., bīstamu vielu, daļiņu un savienojumu nosēdumi ūdenī un to tālāka izplatīšana) monitorings. Tiek analizētas projekta realizācijā iesaistīto valstu likumdošana, pieejamās tehnoloģijas un izglītības, profesionālās un zinātniskās kompetences. Ziņojumā apkopoti sasniegumi un izkliegtā piesārņojuma monitoringa attīstības iespējas, gan projektā iesaistītajās valstīs, gan arī visā Eiropā.

D6.1 Darbības plāns un saistītie biznesa plāni. Eiropas Savienības 7. ietvarprogrammas “Jaunu zināšanu reģionu veidošanās un attīstība” tēmā viens no galvenajiem darbību veidiem ir vienota darbības plāna izveide gan reģionālajā, gan Eiropas līmenī. Baltic Flows projekta ieguldījums minētajā jomā ir strukturēts un aprakstīts šajā dokumentā trīs augstākā līmeņa kategorijās:

1. Pilsoniskā savienība – iesaistīti un iedvesmojoši pilsoņi.
2. Drošas un ērti apdzīvojamās pilsētas Baltijas jūras reģionā un visā Eiropā.
3. Viedā specializācija un sinerģijas starp reģionālo attīstību un izpēti un inovācijām, lai palielinātu konkurētspēju.

Projekts Baltic Flows tika pabeigts 2016. gada septembrī. Vairāk informācijas par to iegūstams tā interneta vietnē www.balticflows.eu



Šis projekts ir saņēmis finansējumu no Eiropas Savienības 7. ietvarprogrammas koordinācijai, atbalstam un kapacitātes stiprināšanai saskaņā ar dotāciju līgumu nr. 319923.